WILEY | Hindawi

Research Article

Macroscale Gas–Water Two-Phase Transport Simulation in Shales considering Nanomicroscale Effects

Dongying Wang [iD],[1,2] **Hua Liu,**[1,2] **Jun Yao,**[3] **Weihong Wang,**[2] **Xiaohu Hu,**[1,2] **and Yanyan Wang**[1,2]

[1]*State Key Laboratory of Shale Oil and Gas Enrichment Mechanisms and Efficient Development, Beijing 102206, China*
[2]*Petroleum Exploration and Production Research Institute, SINOPEC, Beijing 102206, China*
[3]*School of Petroleum Engineering, China University of Petroleum (East China), Qingdao 266580, China*

Correspondence should be addressed to Dongying Wang; dongying.upc@gmail.com

As an effective approach to evaluate shale gas production, macroscale numerical simulations have been conducted; however, multiscale storage space and complex gas–water two-phase transport mechanisms are not systematically considered. To deal with this, a rigorous cross-scale gas–water two-phase transport simulation method that considers the pore, core, and field scale is proposed herein. First, to investigate the fluid storage state in different pore types during the gas–water two-phase transport process, a shale pore network gas–water transport simulation is conducted. Subsequently, a core-scale model that considers the distribution of organic matter is constructed, and the gas–water two-phase transport behaviors are upscaled from the pore to the core by incorporating nanomicroscale effects. Next, a shale gas–water two-phase macroscale numerical simulation is implemented based on the core-scale simulation results. Multiple interacting continua are used to describe the shale matrix and microfractures, whereas the embedded discrete fracture method is employed to represent hydraulic fractures. Finally, the manner by which nanomicroscale effects, stress sensitivity, and SRV area affect the production of shale gas reservoirs is discussed comprehensively. This study provides a practical method to estimate shale gas production by rigorously considering gas–water nanomicroscale effects to reduce uncertainties during productivity evaluation.

1. Introduction

The storage space and fluid transport mechanisms of shale differ significantly from those in conventional gas reservoirs [1–3]. Nanoscale organic pores, nano-micro inorganic pores, and microfractures exist in shale; additionally, millimeter-scale hydraulic fractures are formed after hydraulic fracturing [4–7]. Based on scanning electron microscopy (SEM) images, Loucks et al. [8] observed the inorganic matter (IOM) pore diameters ranged from 35 nm to several microns, whereas the organic matter (OM) pore diameters ranged from 10 to 300 nm. Naraghi et al. [9] statistically analyzed the shape, size, and pore size distributions of various minerals in shale reservoirs and discovered that the OM in shale reservoirs is distributed in a dispersed manner. The classical linear flow law is not applicable to shale owing to

its nanoscale pore size. The current free gas transport models for shale can be classified into two categories. One is the Javadpour model based on the tangential momentum coordination coefficient, and the second is the Civan model based on the Knudsen number (Kn) and slip boundary conditions. Moreover, in OM pores, in addition to free gas transport, surface diffusion occurs in the adsorption layer of the OM surface.

Gas–water two-phase transport occurs during the flowback and production processes in shale gas reservoirs. Based on physical experiments and molecular simulation studies, water transport presents nanomicroscale effects owing to the strong interaction between the water phase and solid wall surface in the nanoscale space. Holt et al. [10] and Majumder et al. [11] discovered that in carbon nanotubes measuring 1.3–7 nm, the measured flow velocity of the water

phase was two to five times that calculated using the Poiseuille equation under nonslip boundary conditions, thus verifying the occurrence of slip in water transport within a confined space. For gas–water two-phase transport, Bennett et al. [12] obtained SEM images of the IOM and discovered a thin water film on the pore wall of the IOM. Bai et al. [13] established a model considering the effect of water film on methane surface diffusion. Implementing gas–water two-phase transport experiments on shale samples is challenging because of their ultralow porosity and permeability. Hence, numerical simulations are typically performed to investigate multiphase transport behavior in shales.

Currently, the most typically used macroscale simulation models to describe fluid flow in fractured media such as shale can be classified into the following three categories: equivalent medium, dual medium, and discrete medium models. The equivalent medium model equates the local effect of fractures on the entire physical model; however, this method is not widely used in shale gas reservoirs because of the oversimplification of the fracture treatment. The dual-media model is more suitable for natural fracture networks with a high degree of development and connectivity; the shale matrix is segmented into a series of multiple interacting continua (MINC) to effectively characterize the unsteady cross-flow between the matrix and fractures [14–16]. However, it is not suitable for locally developed large-scale fractures. Discrete medium models are typically applied to describe hydraulic fractures explicitly. The discrete fracture network (DFN) model only considers fluid flow only in the fracture network [17, 18]. The embedded discrete fracture method (EDFM) is an advanced approach [19, 20], which considers the fluid flow in both matrix and fractures, and the fracture system was directly embedded into the matrix grid in order to simplify the meshing process. Researchers conducted a series of macroscale numerical simulation studies on shale gas reservoirs based on the aforementioned models. Yu et al. [21] used the EDFM to conduct numerical simulations of shale gas reservoirs with multistage fractured horizontal wells while considering gas slip, adsorption, and desorption effects. Huang et al. [22] and Zhang et al. [23] used the MINC model to describe the shale matrix and assigned different physical property parameters to each subdomain in MINC to characterize the heterogeneous characteristics of the shale matrix. Zhang and Emami-Meybodi [24] examined the gas–water two-phase transport patterns at different production stages while considering the effect of stress sensitivity. The variation in shale gas production inside a simulated reservoir volume (SRV) was analyzed by using the double-porosity and double-permeability model by Cao et al. [25]. Farah et al. [26] proposed an effective hybrid approach based on a DFM-MINC proximity function in order to simulate fluid transport behavior in low permeable fractured reservoirs. To date, the upscaling method systematically considering multiscale storage spaces and nanomicroscale effects has not been implemented in shale gas reservoirs. Therefore, the factors above must be considered rigorously when conducting numerical simulations of shale gas, and a cross-scale gas–water two-phase transport simulation method for shale gas reservoirs should be established.

In this study, pore-scale transport simulations are performed using the IOM/OM pore network model incorporating gas–water two-phase transport mechanisms, respectively. Subsequently, the pore-scale transport properties are upscaled to the core scale using a core-scale matrix model that considers stochastically distributed OM. Finally, the upscaling results are substituted into the macroscale model, and the contributions of the nanomicroscale effects and stress sensitivity, as well as the SRV area, are discussed.

2. Gas–Water Two-Phase Transport Behavior considering Nanomicroscale Effect

The complex pore structure, storage mode, and multiple transport mechanisms render the gas–water transport behavior in shale gas reservoirs different from that in conventional gas reservoirs at the pore scale. However, obtaining the shale gas–water two-phase transport behavior in the laboratory is difficult, in particular the properties of the shale matrix. Hence, a rigorous upscaling method was applied to derive the gas–water two-phase transport behavior from the pores to the core in the shale matrix. Subsequently, the core-scale gas–water transport properties can be employed in macroscale simulations. This section introduces a method for upscaling from the pores to the core. A pore-scale gas–water simulation was implemented using a pore network model based on the gas–water nanomicroscale effect. Meanwhile, a core-scale model was established using a Monte Carlo sampling method that considered randomly distributed OM. The core-scale gas–water two-phase transport properties were derived by substituting the pore network model calculation results into the core-scale model.

2.1. Pore-Scale Gas/Water Transport Simulation in Shale Matrix

2.1.1. Gas/Water Single-Phase Transport Behavior. Submicron-sized IOM and OM pores develop in the shale matrix, and the OM pores are typically smaller than 100 nm. As illustrated in Figure 1, IOM pores can be categorized into three shapes: circular, square, and triangular. The OM pores are typically circular, as shown in the SEM images (Figure 1(b)).

The Gangi model [28] is used to describe the stress dependence of the IOM pore radius.

$$r_{\text{in\_stress}} = r_{\text{in0}} \left(\frac{1 - (\sigma_{\text{eff}}/p_1)^m}{1 - (\sigma_{\text{eff0}}/p_1)^m} \right)^{3/5}, \quad (1)$$

$$\sigma_{\text{eff}} = P_{\text{con}} - \alpha_c P, \quad (2)$$

where r_{in0} is the initial IOM pore radius, m; σ_{eff} is the effective stress, Pa; σ_{eff0} is the effective stress under initial condition, Pa; p_1 is the closing pressure, Pa; m is the cementation index, dimensionless; P_{con} represents the confining pressure, Pa; P is the pore pressure, Pa; and α_c denotes the effective stress coefficient, dimensionless.

In addition to the pore size reduction above, pore size enlargement in terms of desorption-induced volume strain
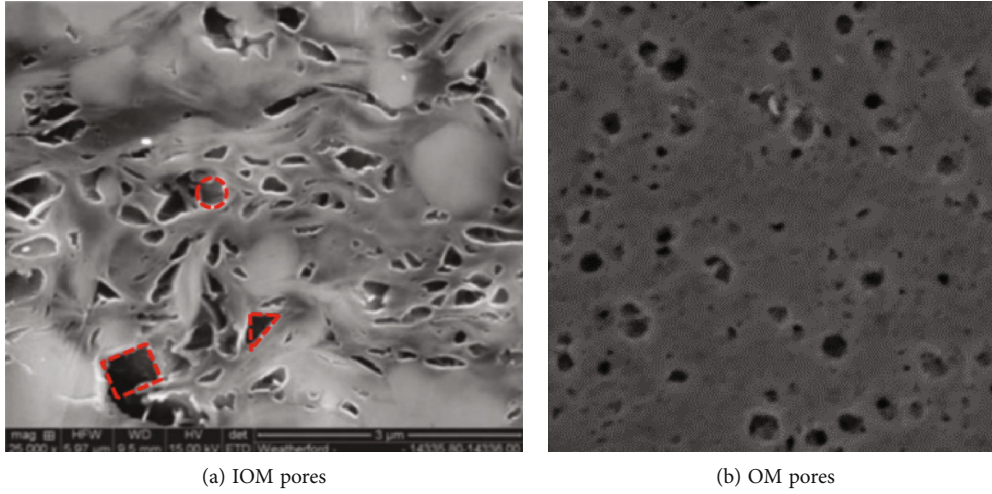
(a) IOM pores

(b) OM pores

FIGURE 1: SEM images of shale IOM and OM pores [27].

occurred in the OM pores. The OM pore size enlargement (dr_{des}) due to OM matrix desorption-induced volume strain can be derived as follows [29]:

$$dr_{des} = r_{or0} \left(\sqrt{1 + \varepsilon_L \frac{P_L(P_0 - P)}{(P + P_L)(P_0 + P_L)} \frac{1 - \phi_{OM}}{\phi_{OM}}} - 1 \right), \quad (3)$$

where P_0 is the initial pore pressure, Pa; r_{or0} is the initial OM pore radius, m; ε_L is the Langmuir strain, dimensionless; and ϕ_{OM} denotes the OM porosity, dimensionless. Hence, the change in the OM pore size due to the poromechanical response and desorption-induced volume strain can be expressed as follows:

$$r_{or\_stress} = r_{or0} \left(\frac{1 - (\sigma_{eff}/p_1)^m}{1 - (\sigma_{eff0}/p_1)^m} \right)^{3/5} + dr_{des}. \quad (4)$$

Gas transport in shale-confined pores is characterized by Kn, which is defined as the ratio of the molecular mean-free path to the characteristic pore length as follows:

$$Kn = \frac{\lambda}{R_c}, \quad (5)$$

$$\lambda = \sqrt{\frac{\pi ZRT}{2M}} \frac{\mu_g}{P}, \quad (6)$$

where Z is the gas compressibility factor, dimensionless; R is the universal gas constant, J/(mol·K); T refers to temperature, K; μ_g is gas viscosity, Pa·s; M represents the gas molecular weight, kg/mol; and P is the pressure, Pa. Meanwhile, R_c is the pore radius for circular pores, length (s) for square pores, and inscribed circle radius (r_{ins}) for triangular pores.

The gas flux in circular pores (q_{cir}) can be determined based on Kn as follows, as proposed by Beskok and Karniadakis [30]:

$$q_{cir} = f_{cir}(Kn_{cir}) \frac{\pi r_{in}^4}{8\mu_g} \frac{\Delta P}{l}, \quad (7)$$

$$f_{cir}(Kn_{cir}) = (1 + \alpha_{cir} Kn_{cir}) \left(1 + \frac{4Kn_{cir}}{1 - \beta Kn_{cir}} \right), \quad (8)$$

$$\alpha_{cir} = \frac{128}{15\pi^2} \tan^{-1} \left[4.0 Kn_{cir}^{0.4} \right], \quad (9)$$

where ΔP is the pressure drop across a single pore, Pa; r_{in} is the radius of circular IOM pore, m; l is the single pore length, m; α_{cir} is the rarefaction coefficient in circular pores, dimensionless; and β is the slip coefficient, dimensionless, where $\beta = -1$.

The gas flux in square pores (q_{squ}) can be expressed as follows [30]:

$$q_{squ} = 0.42173 \frac{s^4}{12\mu_g} \frac{\Delta P}{l} f_{squ}(Kn_{squ}), \quad (10)$$

$$f_{squ}(Kn_{squ}) = (1 + \alpha_{squ} Kn_{squ}) \left(1 + \frac{6Kn_{squ}}{1 - \beta Kn_{squ}} \right), \quad (11)$$

$$\alpha_{squ} = 1.7042 \frac{2}{\pi} \tan^{-1} \left(8 Kn_{squ}^{0.5} \right), \quad (12)$$

where s is the side length of square IOM pores, m, and α_{squ} is the rarefaction coefficient in square pores, dimensionless.

The ratio of the fluid flux in a triangular pore to that in a circular pore, whose radius is equal to the inscribed circular radius of the triangular pore, can be expressed as follows:

$$\frac{q_{tri}}{q_{cir}} = \frac{18\sqrt{3}}{5\pi}. \quad (13)$$

Hence, the gas flux in triangular pores (q_{tri}) can be expressed as follows [31]:

$$q_{\text{tri}} = \frac{9\sqrt{3}r_{\text{ins}}^4}{20\mu_{\text{g}}} \frac{\Delta P}{l} f_{\text{cir}}(Kn_{\text{cir}}), \tag{14}$$

where r_{ins} is the inscribed circle radius for triangular IOM pores, m.

The fluid transport conductance is defined as the fluid flux at a unit pressure drop. The single-phase gas transport conductance in IOM pores of different shapes can be derived using Eqs. (15)–(17) based on Darcy's law.

$$g_{\text{in\_cir}} = \frac{r_{\text{in}}^4}{8\mu_{\text{g}}l}\left(1 + \frac{128}{15\pi^2}\tan^{-1}\left[4.0Kn_{\text{cir}}^{0.4}\right]Kn_{\text{cir}}\right)\left(1 + \frac{4Kn_{\text{cir}}}{1 + Kn_{\text{cir}}}\right), \tag{15}$$

$$g_{\text{in\_squ}} = 0.42173\frac{s^4}{12\mu_{\text{g}}l}\left(1 + 1.7042\frac{2}{\pi}\tan^{-1}\left[8Kn_{\text{squ}}^{0.5}\right]Kn_{\text{squ}}\right) \\ \cdot \left(1 + \frac{6Kn_{\text{squ}}}{1 + Kn_{\text{squ}}}\right), \tag{16}$$

$$g_{\text{in\_tri}} = \frac{9\sqrt{3}r_{\text{ins}}^4}{20\mu_{\text{g}}l}\left(1 + \frac{128}{15\pi^2}\tan^{-1}\left[4.0Kn_{\text{cir}}^{0.4}\right]Kn_{\text{cir}}\right) \\ \cdot \left(1 + \frac{4Kn_{\text{cir}}}{1 + Kn_{\text{cir}}}\right). \tag{17}$$

In the OM pores, in addition to bulk gas transport, which can be characterized by Eq. (15), the surface diffusion is not negligible owing to gas adsorption in the OM. The adsorbed gas surface diffusion in the OM pores can be expressed as follows [32]:

$$g_{\text{or\_sur}} = \frac{M}{\rho_{\text{g}}l}D_{\text{s}}C_{\text{amax}}\frac{d\theta_{\text{c}}}{dP}\pi\left(r_{\text{or}}^2 - r_{\text{or\_eff}}^2\right), \tag{18}$$

$$C_{\text{amax}} = \frac{C_{\text{max}}}{\text{TOC}}, \tag{19}$$

$$\theta_c = \frac{P/Z}{P/Z + P_{\text{L}}}, \tag{20}$$

$$r_{\text{or\_eff}} = r - d_{\text{m}}\theta_{\text{c}}, \tag{21}$$

where D_{s} is the surface diffusion coefficient, m^2/s; C_{max} is the maximum adsorbed gas concentration in the shale core, mol/m^3; C_{amax} is the maximum adsorbed gas concentration in the OM pores, mol/m^3; TOC is the total organic carbon content, dimensionless; P_{L} is the Langmuir pressure, Pa; θ_{c} is the gas coverage, dimensionless; and d_{m} is the gas molecular diameter, m. Hence, the total gas transport conductance in the OM pores can be obtained as the superimposition of the bulk gas transport and surface diffusion as follows:

$$g_{\text{or}} = \frac{r_{\text{or\_eff}}^4}{8\mu_{\text{g}}l}\left(1 + \frac{128}{15\pi^2}\tan^{-1}\left[4.0Kn_{\text{cir}}^{0.4}\right]Kn_{\text{cir}}\right) \\ \cdot \left(1 + \frac{4Kn_{\text{cir}}}{1 + Kn_{\text{cir}}}\right) + \frac{M}{\rho_{\text{g}}l}D_{\text{s}}C_{\text{amax}}\frac{d\theta_{\text{c}}}{dP}\pi\left(r_{\text{or}}^2 - r_{\text{or\_eff}}^2\right). \tag{22}$$

For single-phase water transport in IOM/OM pores, the water slip along the pore surface is not negligible, and the slip length can be expressed as a function of the wetting angle as follows [32]:

$$l_{\text{s}} = \frac{0.41}{(\cos\theta + 1)^2} \times 10^{-9}, \tag{23}$$

where θ is the wetting angle.

The water transport conductance in the IOM/OM circular pores considering water slip is derived as follows [32]:

$$g_{\text{in(or)\_cir\_w}} = \frac{\pi}{8\mu_{\text{w}}l}\left(r_{\text{in}}^4 + 4r_{\text{in}}^3l_{\text{s}}\right), \tag{24}$$

where $g_{\text{in(or)\_cir\_w}}$ is the water transport conductance in the IOM and OM circular pores, m^3/(s·Pa), and the water viscosity (μ_{w}) is expressed as a function of temperature as follows [33]:

$$\mu_{\text{w}}(T) = 2.414 \times 10^{-5} \times 10^{247.8/(T-140)}. \tag{25}$$

The ratio of fluid flux in the square pores to that in the circular pores under the same inscribed radii can be obtained as follows [31]:

$$\frac{q_{\text{squ}}}{q_{\text{cir}}} = \frac{4.4984}{\pi}. \tag{26}$$

Hence, the water conductance in the IOM square pores is expressed as follows:

$$g_{\text{in\_squ\_w}} = \frac{4.4984}{8\mu_{\text{w}}l}\left(r_{\text{ins\_squ}}^4 + 4r_{\text{ins\_squ}}^3l_{\text{s}}\right), \tag{27}$$

where $r_{\text{ins\_squ}}$ is the inscribed radii of the square pores, m. Similarly, the water conductance in the IOM triangular pores can be expressed by combining Eq. (13) as follows:

$$g_{\text{in\_tri\_w}} = \frac{9\sqrt{3}}{20}\frac{1}{\mu_{\text{w}}l}\left(r_{\text{ins\_tri}}^4 + 4r_{\text{ins\_tri}}^3l_{\text{s}}\right), \tag{28}$$

where $r_{\text{ins\_tri}}$ is the inscribed radii of the triangular pores, m.

In this study, IOM and OM were investigated separately at the pore scale owing to their different fluid storage types and complex fluid transport mechanisms. The pore network model can accurately describe the distribution of nanopores in shale and is an effective approach for pore-scale fluid flow simulation; hence, IOM and OM pore network models were established based on SEM images of IOM and focusing-ion-
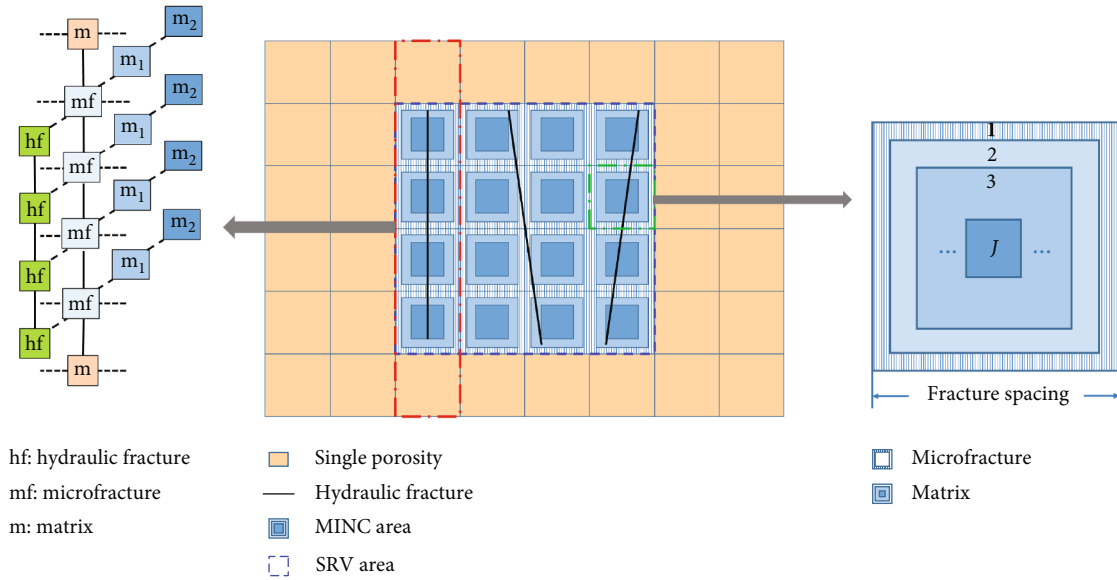
FIGURE 2: Grid structure coupling matrix, microfractures, and hydraulic fractures.
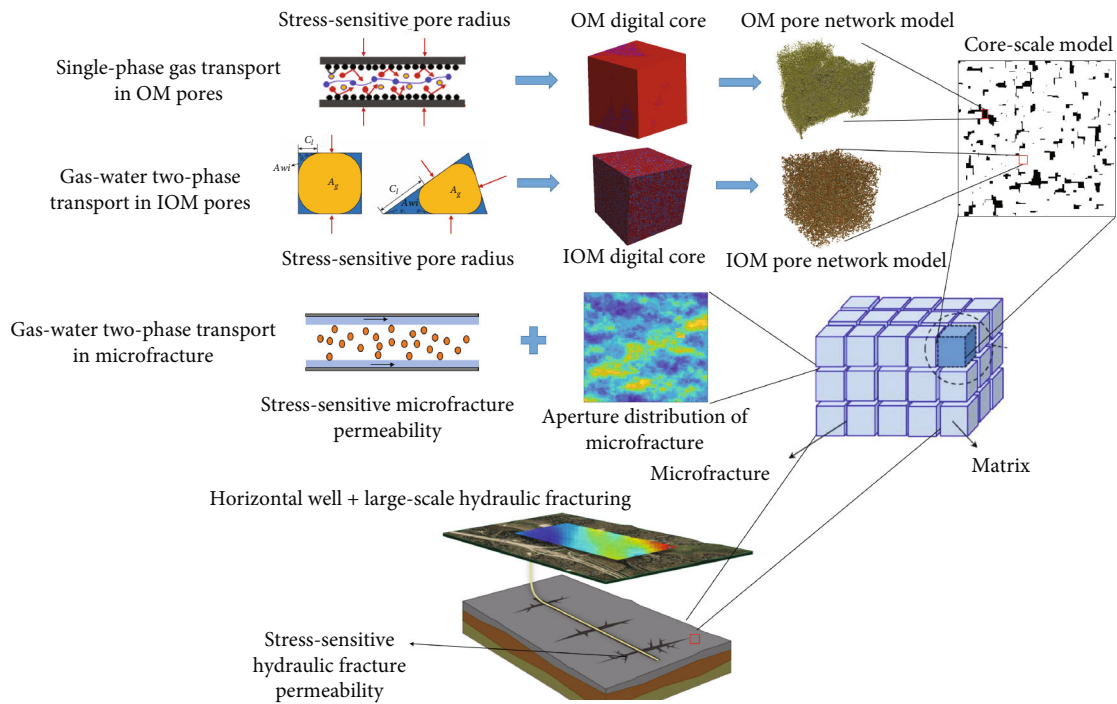

FIGURE 3: Technical workflow for macroscale numerical simulation of shale gas reservoir.

beam scanning electron microscope (FIB-SEM) images of OM, respectively. The IOM/OM digital cores were reconstructed, and the pore network models can be extracted using the maximal ball-fitting method.

For a constant pressure drop between the inlet and outlet of the pore network model combined with fluid mass conservation in each pore (Eqs. (29)–(31)), the pressure distribution of the IOM/OM pore network can be obtained as follows:

$$\sum_{j=1}^{N_i} q_{ij} = 0, \tag{29}$$

$$q_{ij} = g_{ij}(P_i - P_j), \tag{30}$$

$$\frac{1}{g_{ij}} = \frac{1}{g_i} + \frac{1}{g_t} + \frac{1}{g_j}, \tag{31}$$
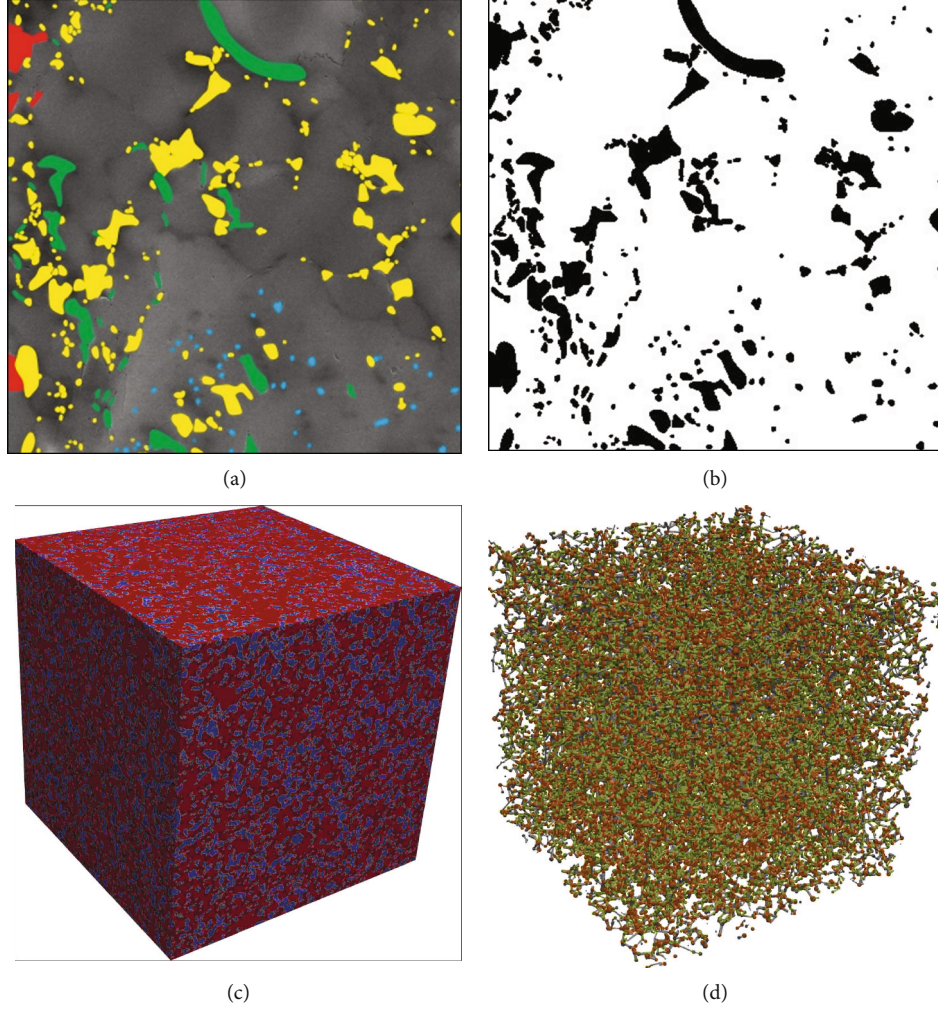
(a)

(b)

(c)

(d)

FIGURE 4: Images of IOM. (a) SEM image, (b) binary SEM image, (c) 3D digital core, and (d) pore network model (yellow represents intergranular pores, red represents dissolution pores, green represents narrow pores in (a), black represents pores in (b), red represents the matrix, and purple represents pores in (c); red spheres represents pores and throats, which are described by green lines in (d)).

where N_i is the number of pores connected with pore i; q_{ij} is the flux between pore i and pore j, m$^3 \cdot$s^{-1}; P_i and P_j are the pressure of pore i and j, respectively, Pa; g_{ij} presents the conductance between pore i and pore j, m$^3 \cdot$Pa$^{-1} \cdot$s^{-1}; and g_i, g_t, and g_j are the conductance of pore i, throat t, and pore j, respectively, m$^3 \cdot$Pa$^{-1} \cdot$s^{-1}.

The single-phase gas/water permeability ($k_{a\_g(w)}$) was derived based on Darcy's law as follows:

$$k_{a\_g(w)} = \frac{\sum_{i=1}^{N_{outlet}} q_{outlet} \mu_g L_{net}}{A_{outlet} \Delta P_{net}}, \tag{32}$$

where q_{outlet} is the flux of each pore at the outlet in the pore network model, m$^3 \cdot$s^{-1}; L_{net} is the size along the flow direction in the pore network model, m; A_{outlet} is the cross-sectional area at the outlet of the pore network model, m^2; ΔP_{net} is the pressure difference between the two ends of the pore network model, Pa; and N_{outlet} is the number of pores at the outlet of the pore network model.

2.1.2. Gas–Water Two-Phase Transport Behavior.

Water imbibes into shale IOM pores during the hydraulic fracturing process, and results from the IOM surface are water-wetting, while the OM surface is gas-wetting. In this case, the gas displacing water process occurs in IOM pores and only single-phase gas transport in OM pores during flowback and production. In the IOM circular pores, gas completely displaces water once the displacement pressure reaches the threshold capillary pressure. However, for the square and triangular IOM pores, gas begins to enter the pores when the displacement pressure is equal to the threshold capillary pressure, and water is transported in the corners, whereas gas is transported to the center. Subsequently, the area occupied by the corner water is continuously compressed as the displacement pressure increases. A detailed method for calculating the area occupied by water and gas in the square and triangular pores during the gas–water two-phase transport process is provided in the related work [32].

The water and gas transport conductances in the irregular IOM pores (square and triangular pores) are obtained by
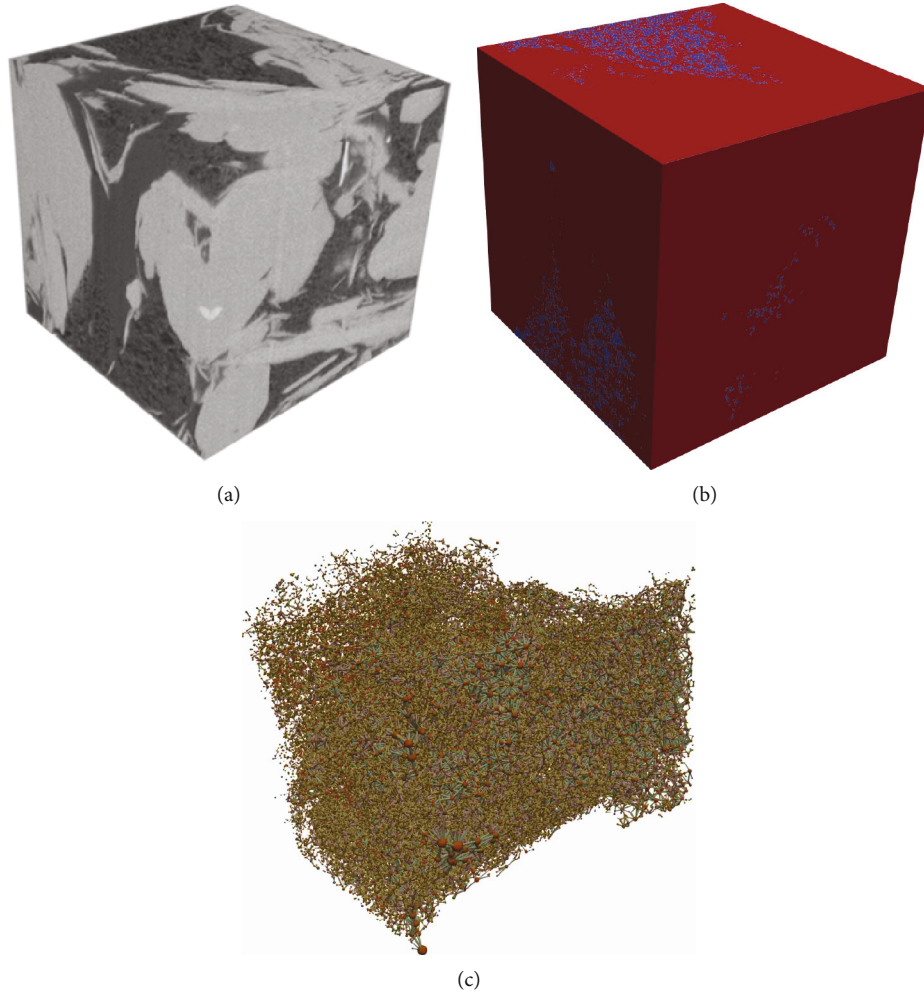
(a)

(b)

(c)

FIGURE 5: Images for OM. (a) FIB-SEM image, (b) 3D digital core, and (c) pore network model.

multiplying the single-phase gas/water conductance by the cross-sectional area occupied by gas and water as follows:

$$g_{in\_squ(tri)\_gm} = \frac{A_g}{A} g_{in\_squ(tri)\_g}, \tag{33}$$

$$g_{in\_squ(tri)\_wm} = \frac{A_w}{A} g_{in\_squ(tri)\_w}, \tag{34}$$

where $g_{in\_squ(tri)\_gm}$ and $g_{in\_squ(tri)\_wm}$ are the gas and water conductances, respectively, during the gas–water two-phase transport process in the square or triangular pores, m³/(s·Pa); A_g and A_w are the cross-sectional areas occupied by gas and water, respectively, and $g_{in\_squ(tri)\_g}$ and $g_{in\_squ(tri)\_w}$ are the single-phase gas and water conductance, respectively, in the square and triangular pores, m³/(s·Pa).

Gas–water two-phase transport is achieved via invasion percolation using the IOM pore network model. The IOM pore network is initially saturated with water, and the gas first displaces water in relatively large pores owing to the wettability. Water in the smaller pores is gradually displaced by gas as the displacement pressure increases, and the area occupied by corner water in the irregular pores (square

TABLE 1: Model parameters for IOM/OM pore networks.

Simulation parameter	Value
Pressure (P/MPa)	40
Temperature (T/K)	400
Water critical temperature (T_{c_w}/K)	641.4
Universal gas constant (R/(J·mol⁻¹·K⁻¹))	8.314
IOM contact angle (θ_{IOM}/°)	30
OM contact angle (θ_{OM}/°)	120
Pressure gradient (dP/dx/(MPa·m⁻¹))	0.1
Langmuir Pressure (P_L/MPa)	13.789514
Maximum adsorbed gas concentration in the total core (C_{max}/(m³·mol⁻¹)	328.7
Isosteric adsorption heat at zero gas coverage ($\Delta H(0)$ /(J·mol⁻¹))	16000
Ratio of blockage rate constant to forward movement rate constant (κ /dimensionless)	0.5
Linear change coefficient of Isothermal adsorption heat (δ/(J·mol⁻¹))	-4186

(a) IOM averaged pore size change

(b) OM averaged pore size change
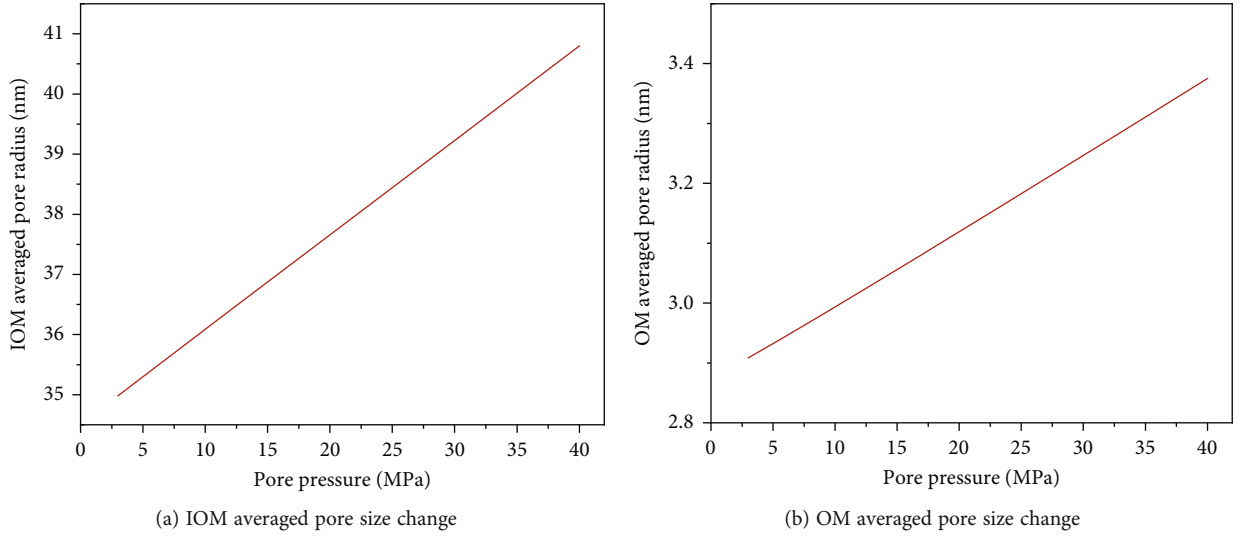
FIGURE 6: Variation of averaged pore radius in IOM and OM with different pore pressures.

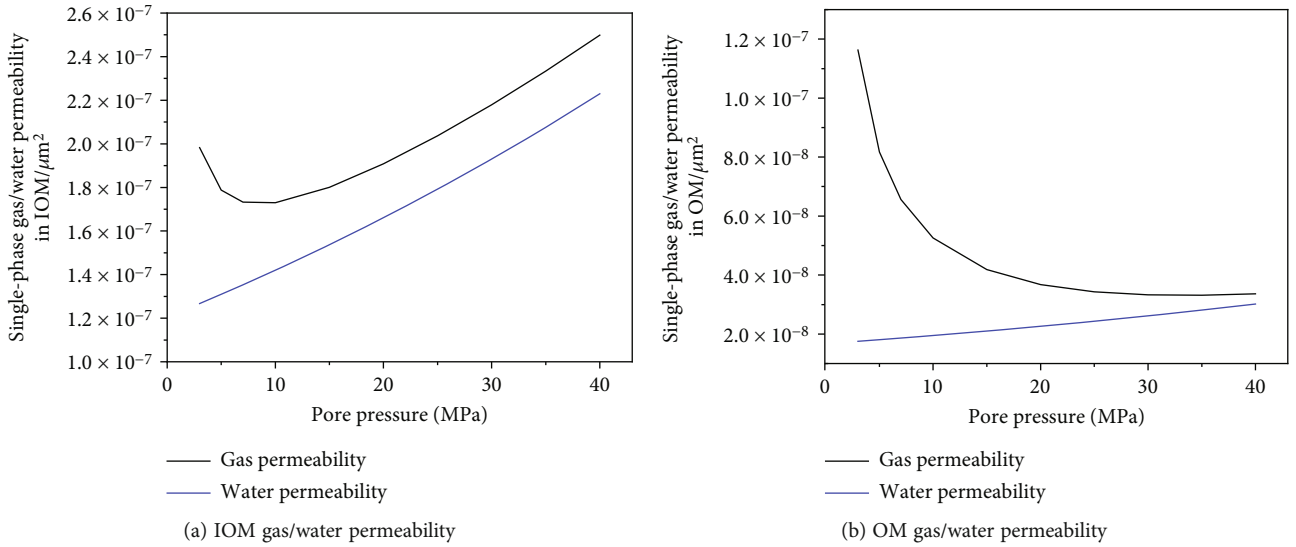(a) IOM gas/water permeability

(b) OM gas/water permeability

FIGURE 7: Variation of averaged gas and water permeabilities in IOM and OM with different pore pressures.

and triangular pores) is compressed. Water saturation in the IOM pore network model (S_{w_IOM}) can be expressed as follows:

$$S_{w\_IOM} = \frac{\sum_{i=1}^{n_1} V_{pi} + \sum_{i=1}^{n_2} V_{ci}}{V_t}, \tag{35}$$

where V_{pi} is the volume of a pore that is not invaded by gas, m^3; V_{ci} is the volume occupied by water in the corner of the IOM square or triangular pores that have been invaded by gas, m^3; n_1 denotes the number of pores not occupied by gas; n_2 is the number of IOM square or triangular pores that have been invaded by gas; and V_t is the total pore volume of the IOM pore network model, m^3.

The water conductance in the circular, square, and triangular pores that have not been invaded by gas can be

expressed by Eqs. (24), (27), and (28). For pores invaded by gas, the gas conductance can be expressed using Eqs. (15), (33), and (34), whereas water conductance in square and triangular pores are expressed as shown in Eqs. (33) and (34). The pressure distribution of the IOM pore network model during the gas-displacing water process can be obtained using Eqs. (29)–(31). Hence, the effective gas and water permeabilities (k_{eff_g} and k_{eff_w}, respectively) can be derived using Eqs. (36) and (37), respectively.

$$k_{eff\_g} = \frac{\sum_{i=1}^{N_{outlet}} q_{outlet\_g} \mu_g L_{net}}{A_{outlet} \Delta P_{net}}, \tag{36}$$

$$k_{eff\_w} = \frac{\sum_{i=1}^{N_{outlet}} q_{outlet\_w} \mu_w L_{net}}{A_{outlet} \Delta P_{net}}, \tag{37}$$

(a) Capillary pressure in IOM
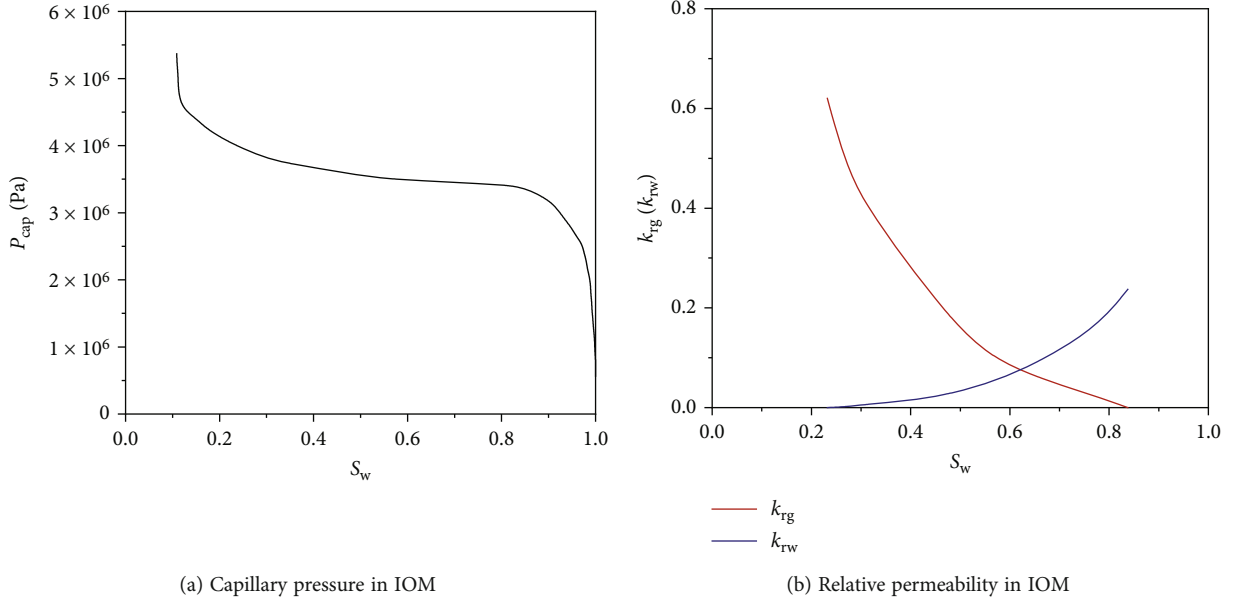

(b) Relative permeability in IOM

FIGURE 8: Gas–water two-phase transport behavior in IOM pore network model.

where $q_{\text{outlet\_g}}$ and $q_{\text{outlet\_w}}$ are the gas and water flux, respectively, in a single pore at the outlet of the IOM pore network model, $m^3 \cdot s^{-1}$.

Hence, the gas–water two-phase relative permeability can be derived as follows:

$$k_{\text{rg}} = \frac{k_{\text{eff\_g}}}{k_{\text{a\_g}}}, \tag{38}$$

$$k_{\text{rw}} = \frac{k_{\text{eff\_w}}}{k_{\text{a\_w}}}. \tag{39}$$

2.2. Core-Scale Gas/Water Transport Simulation in Shale Matrix

2.2.1. Core-Scale Model Construction. The shale matrix exhibited strong heterogeneity owing to the randomly distributed IOM and OM. Hence, a core-scale model was established by considering stochastically distributed OM patches using the Monte Carlo sampling method. Details regarding the core-scale model construction method are available in our previous publication [34]. The core-scale model is generated using randomly distributed IOM patches whose size is equal to that of the corresponding IOM pore network model. Moreover, based on our previous study, the representative elementary size of the shale core-scale model was determined to be $420\,\mu m \times 420\,\mu m$ [34]. Hence, a core-scale model measuring $420\,\mu m \times 420\,\mu m$ was established in this study.

2.2.2. Single-Phase Gas/Water Transport Properties Calculation of Core-Scale Model. The governing equation for single-phase gas/water transport in the core-scale model can be expressed as follows:
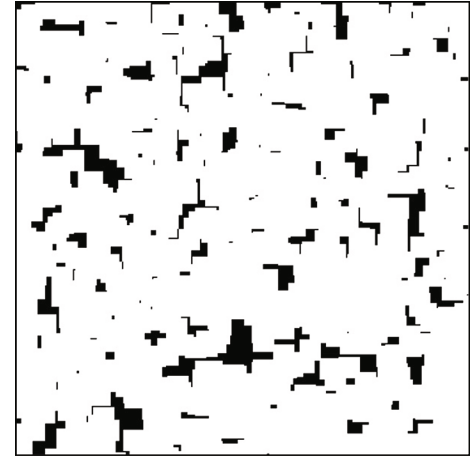

FIGURE 9: Shale matrix core-scale model.

$$\frac{\partial}{\partial x}\left(\frac{k_{x(g/w)}}{\mu_{g/w}} \cdot \frac{\partial P}{\partial x}\right) + \frac{\partial}{\partial y}\left(\frac{k_{y(g/w)}}{\mu_{g/w}} \cdot \frac{\partial P}{\partial y}\right) = 0, \tag{40}$$

where $k_{x(g/w)}$ and $k_{y(g/w)}$ are the single-phase gas/water permeability in the X- and Y-directions, respectively, μm^2, and $\mu_{g/w}$ is the viscosity of gas or water, Pa·s. The local permeability of the single-phase gas/water of IOM/OM patches in the core-scale model is represented using the corresponding calculation results based on the IOM/OM pore network model. A single-phase gas or water pressure distribution can be derived by solving the governing equation using the finite difference method. Subsequently, the core-scale single-phase gas/water permeability can be calculated using Darcy's law.
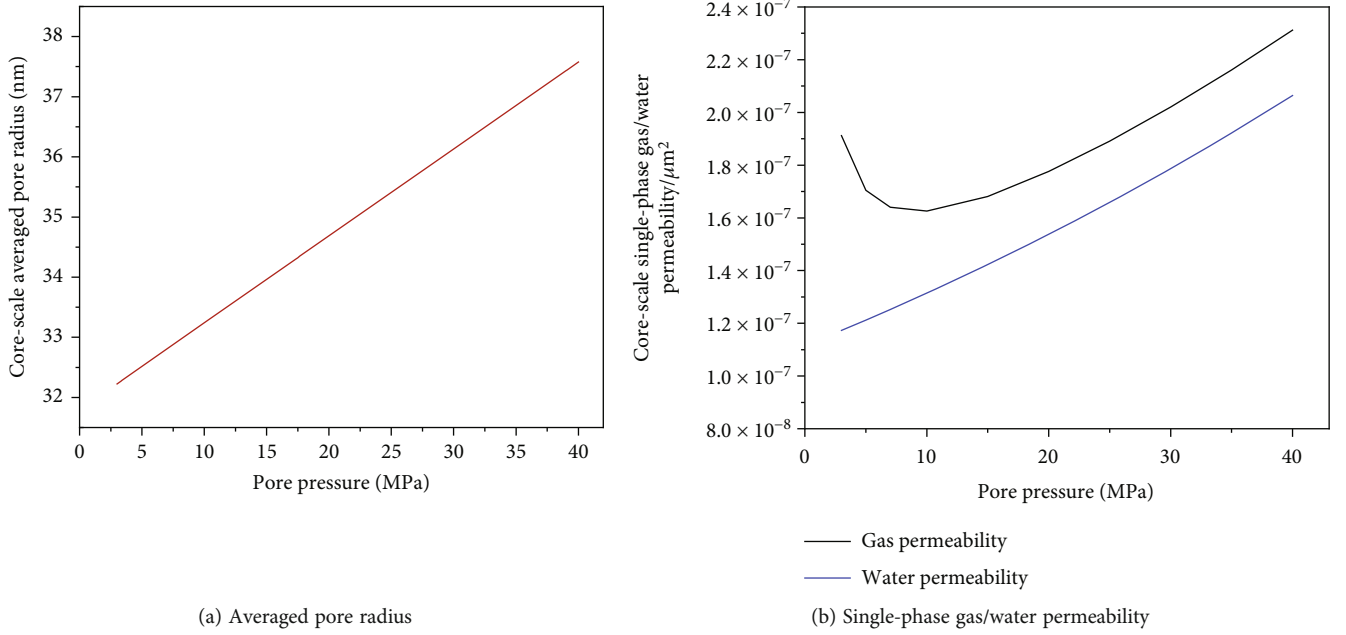
(a) Averaged pore radius

(b) Single-phase gas/water permeability

FIGURE 10: Variations in core-scale averaged pore radius and single-phase gas/water permeability with pore pressure.
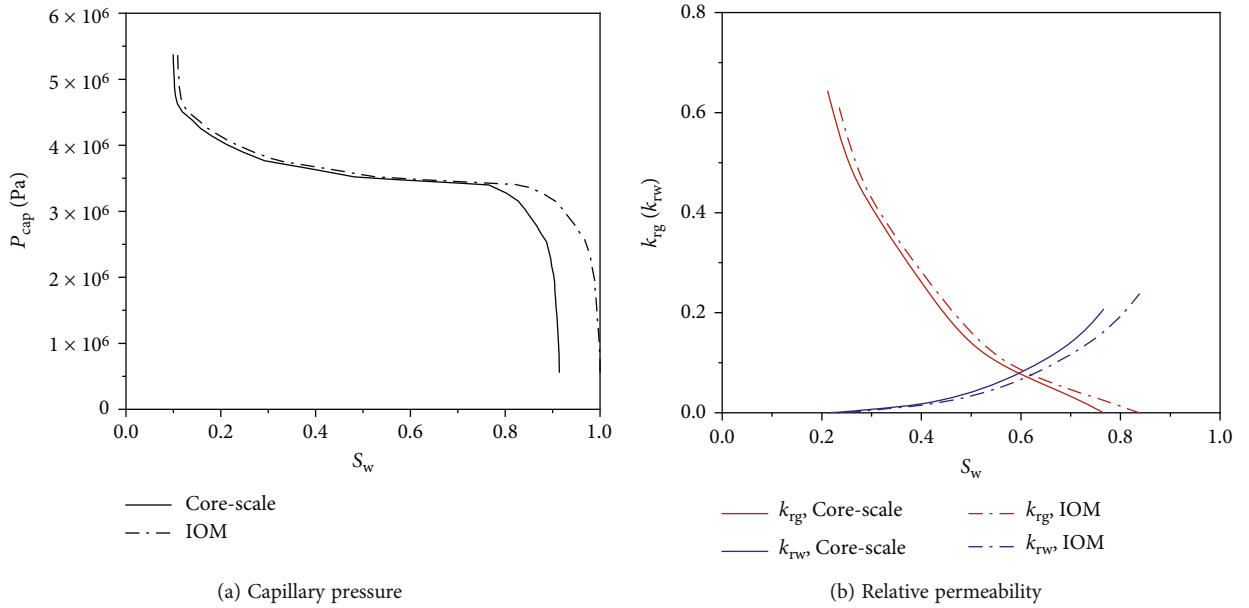

(a) Capillary pressure

(b) Relative permeability

FIGURE 11: Core-scale capillary pressure and gas–water relative permeability curves.

2.2.3. Gas–Water Two-Phase Transport Properties of Core-Scale Model. Owing to the wettability difference between the IOM and OM mentioned above, single-phase gas transport in the OM and gas–water two-phase transport in the IOM occurred after gas injection in the core-scale model. The injection pressure was increased from the lowest capillary pressure in the entire core-scale model, and each injection pressure corresponded to a specific water saturation and gas/water effective permeability in the IOM patch. The governing equations for gas–water two-phase transport at the core-scale can be expressed as follows:

$$\frac{\partial}{\partial x}\left(\frac{k_{\text{eff\_g\_x}}}{\mu_{\text{g}}} \cdot \frac{\partial P_{\text{g}}}{\partial x}\right) + \frac{\partial}{\partial y}\left(\frac{k_{\text{eff\_g\_y}}}{\mu_{\text{g}}} \cdot \frac{\partial P_{\text{g}}}{\partial y}\right) = 0, \quad (41)$$

$$\frac{\partial}{\partial x}\left(\frac{k_{\text{eff\_w\_x}}}{\mu_{\text{w}}} \cdot \frac{\partial P_{\text{w}}}{\partial x}\right) + \frac{\partial}{\partial y}\left(\frac{k_{\text{eff\_w\_y}}}{\mu_{\text{w}}} \cdot \frac{\partial P_{\text{w}}}{\partial y}\right) = 0, \quad (42)$$

where $k_{\text{eff\_g\_x}}$ and $k_{\text{eff\_g\_y}}$ are the gas effective permeabilities in the X- and Y-directions, μm^2, where $k_{\text{eff\_g\_x}} = k_{\text{eff\_g\_y}}$; $k_{\text{eff\_w\_x}}$ and $k_{\text{eff\_w\_y}}$ are the water effective permeabilities in

the X- and Y-directions, respectively; μm^2, where $k_{eff\_w\_x} = k_{eff\_w\_y}$; μ_g and μ_w are the viscosities of gas and water, respectively, Pa·s; and P_w and P_g are the water and gas pressures, respectively, Pa. The effective gas and water permeabilities in the local IOM of the core-scale model are expressed as follows:

$$k_{eff\_g\_x(y)} = k_{eff\_g\_IOM}(P_{cap}), \tag{43}$$

$$k_{eff\_w\_x(y)} = k_{eff\_w\_IOM}(P_{cap}). \tag{44}$$

Here, $k_{eff\_g\_IOM}(P_{cap})$ and $k_{eff\_w\_IOM}(P_{cap})$ are the corresponding gas and water effective permeabilities, respectively, under a specific injection pressure in the core-scale model, μm^2.

Similarly, the gas and water effective permeabilities in the local OM of the core-scale model can be expressed as follows:

$$k_{eff\_g\_x(y)} = k_{abs\_g\_OM}, \tag{45}$$

$$k_{eff\_w\_x(y)} = 0, \tag{46}$$

where $k_{abs\_g\_OM}$ is the single-phase gas permeability obtained from the OM pore network model, μm^2.

The gas–water two-phase pressure distribution of the core-scale model can be derived using the finite difference method combined with initial and boundary conditions, as follows:

$$P_0(x, y) = P_i, \tag{47}$$

$$P^{(g/w)}(0, y) = P_{inlet}, \tag{48}$$

$$P^{(g/w)}(L_x, y) = P_{outlet}, \tag{49}$$

$$\left(\frac{\partial P_{(g/w)}}{\partial y}\right)_{y=0} = 0, \tag{50}$$

$$\left(\frac{\partial P_{(g/w)}}{\partial y}\right)_{y=L_y} = 0, \tag{51}$$

where $P_{(g/w)}$ represents the gas or water pressure, Pa.

The gas–water relative permeabilities can be calculated using Eqs. (38) and (39). The water saturation of the core-scale model (S_w) can be expressed as follows:

$$S_w = (1 - TOC) \cdot S_{w\_IOM}(P_{cap}). \tag{52}$$

The validity of the gas–water two-phase transport behavior simulation based on the core-scale model has been confirmed in our previous study [32]. Moreover, the gas–water relative permeability considering the stress sensitivity can be obtained via core-scale simulations under different pore
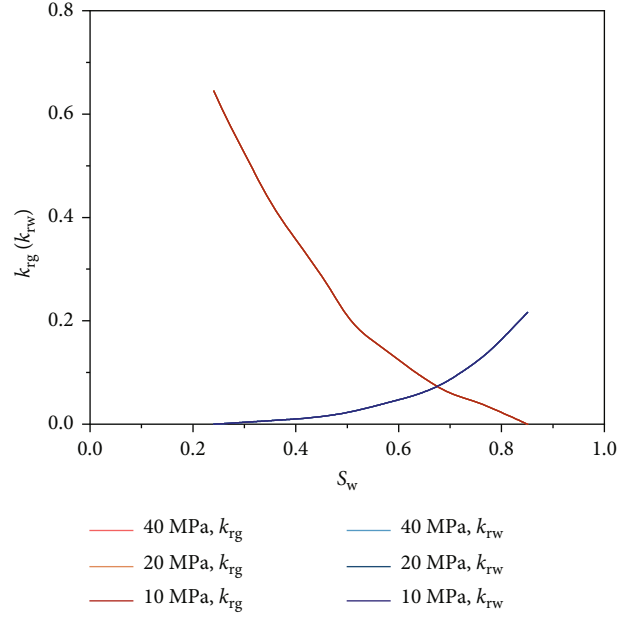

FIGURE 12: Core-scale gas–water relative permeability curves at different pore pressures.
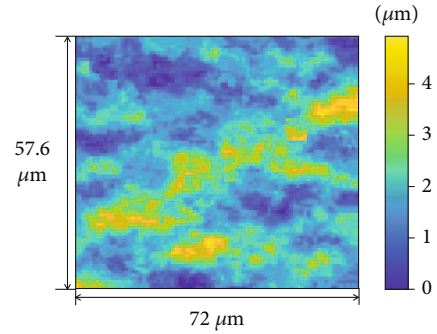

FIGURE 13: Aperture distribution of a real microfracture from a specific shale basin in China.

pressures. The capillary pressure at different pore pressures can be updated using the following equation:

$$P_{cap} = P_{cap0} \frac{r_{in0}}{r_{in\_stress}}, \tag{53}$$

where P_{cap0} is the capillary pressure under the initial condition, Pa, and r_{in_stress} can be obtained from Eq. (1).

2.3. Gas–Water Two-Phase Transport Behavior in Microfracture and Hydraulic Fracture.

To distinguish between hydraulic fractures and microfractures, between which the latter are smaller than the former, the calculation approach of microfracture relative permeability in our previous study is applied in this work [35]. We have noticed that the capillary pressure in microfracture is much smaller than that of matrix; hence, the capillary pressure in microfracture is ignored during macroscale simulation. The gas–water

(a) Relative permeability

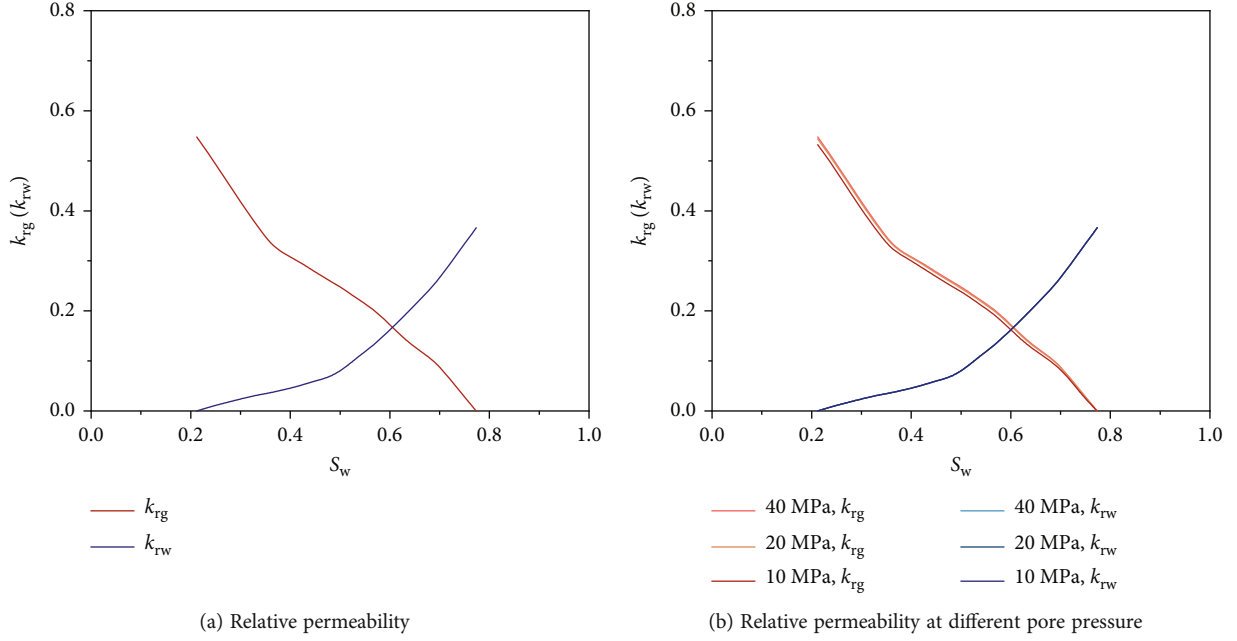(b) Relative permeability at different pore pressure

FIGURE 14: Relative permeability of microfracture and its change with pore pressure.

two-phase relative permeability in hydraulic fractures is presented by the "X"-type relative permeability curve, and the capillary pressure is disregarded.

The permeability of microfractures and hydraulic fractures considering stress sensitivity can be expressed as follows [36]:

$$k_{\mathrm{f}} = k_{\mathrm{f0}} e^{-a_{\mathrm{s,f}}(\sigma_{\mathrm{eff0}} - \sigma_{\mathrm{eff}})}, \qquad (54)$$

where k_{f} and k_{f0} are the current and initial permeabilities of microfracture or hydraulic fracture, respectively, μm^2, and $a_{\mathrm{s,f}}$ is the stress sensitivity coefficient, Pa^{-1}.

3. Macroscale Gas–Water Two-Phase Transport Simulation Method

Regarding the production mode of "horizontal well + large-scale hydraulic fracturing" in shale gas reservoir, MINC is used to describe the matrix and microfractures, whereas hydraulic fractures are described by the embedded discretized fracture using the EDFM. A mathematical model of macroscale gas–water two-phase transport in a shale gas reservoir is established and solved.

3.1. Gas–Water Two-Phase Transport Mathematical Model. Considering the formation of water and fracturing fluid during shale gas reservoir development, the gas–water two-phase transport governing equations for shale gas reservoirs are expressed as follows:

$$-\nabla \cdot \left(\rho_{\mathrm{g}} \mathbf{v}_{\mathrm{g},\chi}\right) + q_{\mathrm{g},\chi} = \frac{\partial \left(\phi_\chi \rho_{\mathrm{g}} S_{\mathrm{g},\chi} + \delta_{\mathrm{m}} q_{\mathrm{ads}}\right)}{\partial t}, \qquad (55)$$

$$-\nabla \cdot \left(\rho_{\mathrm{w}} \mathbf{v}_{\mathrm{w},\chi}\right) + q_{\mathrm{w},\chi} = \frac{\partial \left(\phi_\chi \rho_{\mathrm{w}} S_{\mathrm{w},\chi}\right)}{\partial t}, \qquad (56)$$

where the subscripts g and w represent gas and water, respectively; $\chi = m$, mf, and hf represent the matrix, microfracture, and hydraulic fracture, respectively; V is the transport velocity, m/s; and q_{ads} refers to shale gas adsorption, kg/m³. For the matrix, $\delta_{\mathrm{m}} = 1$; for the microfracture and hydraulic fracture, $\delta_{\mathrm{m}} = 0$. ϕ_χ denotes the porosity; $S_{g,\chi}$ and $S_{\mathrm{w},\chi}$ denote the saturation of gas and water in different media, respectively; $q_{\mathrm{g},\chi}$ and $q_{\mathrm{w},\chi}$ are source and sink items caused by injection and development, respectively, kg/(m³·s); and ρ_{g} and ρ_{w} are the gas and water density. Gas density is provided in our work [32], and the water density can be expressed as follows:

$$\rho_{\mathrm{w}} = \rho_{\mathrm{w0}} e^{c_{\mathrm{w}}(P_{\mathrm{w}} - P_{\mathrm{w0}})}, \qquad (57)$$

where ρ_{w0} represents the initial water density at the initial pressure, kg/m³; P_w is the water pressure, Pa; and c_{w} is the water compressibility, Pa^{-1}.

The fluid transport velocity V can be expressed based on Darcy's law as follows:

$$\mathbf{v}_{\beta,\chi} = -\frac{k_{\beta,\chi}(P) k_{\mathrm{r}\beta,\chi}(P)}{\mu_\beta} \nabla \psi_\beta, \qquad (58)$$

where $k_{\beta,\chi}(P)$ is the single-phase permeability considering the nanomicroscale effect, μm^2, which can be obtained from core-scale transport simulation; $k_{\mathrm{r}\beta,\chi}(P)$ is the relative permeability of different media; $k_{\beta,\chi}(P)$ and $k_{\mathrm{r}\beta,\chi}(P)$ are both pressure dependent, which can be obtained from Section 2;

(a) Conceptual model of shale gas reservoir
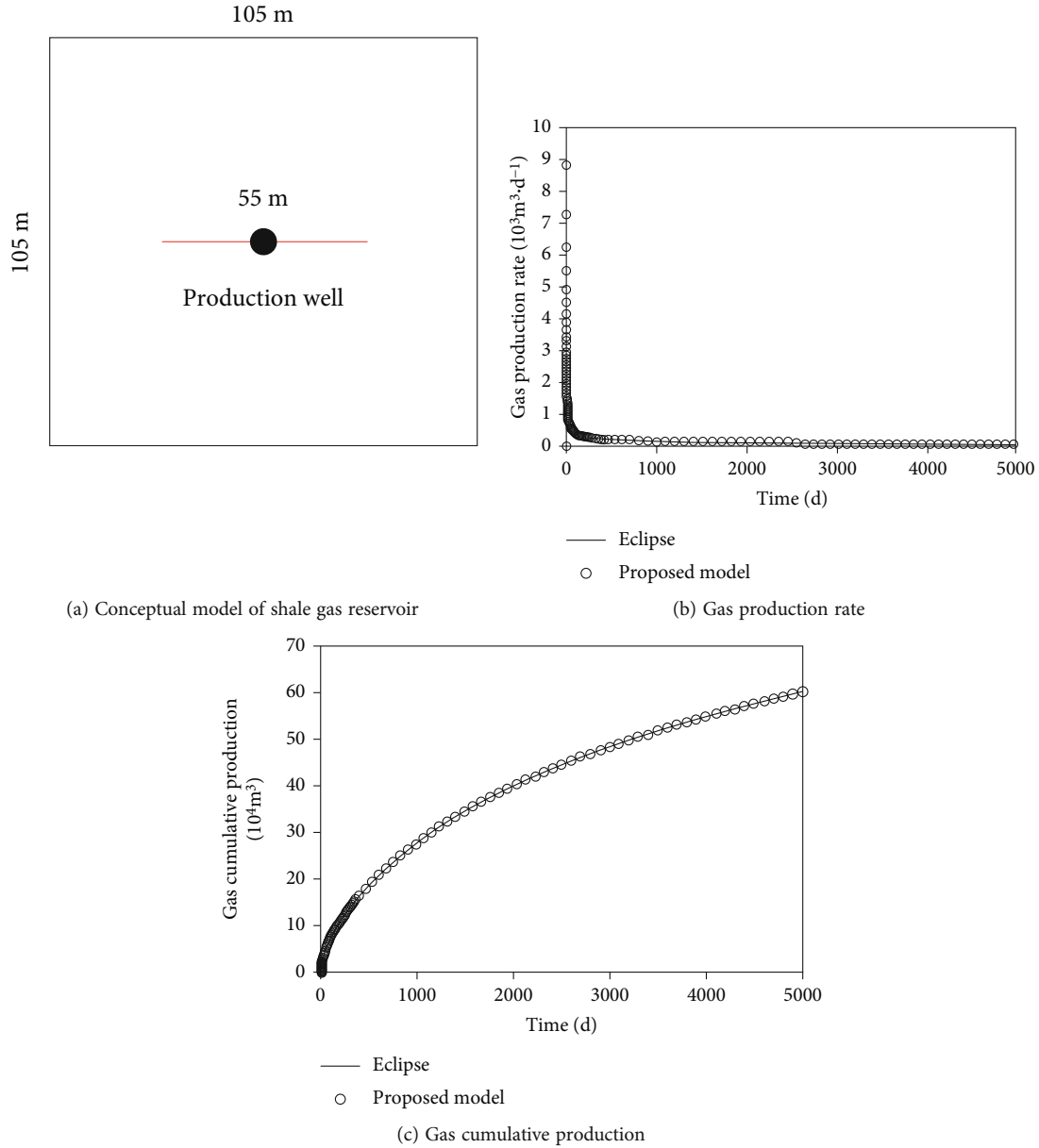
(b) Gas production rate

(c) Gas cumulative production

FIGURE 15: Conceptual shale gas reservoir model and model validation.

ψ is the fluid transport potential, expressed as $\psi = P - \rho g D$, Pa; and D is the depth, m.

The adsorption item q_{ads} can be expressed as follows based on the Langmuir isotherm:

$$q_{ads} = \rho_r \rho_{gstd} V_L \frac{P_g/Z}{P_L + P_g/Z}, \qquad (59)$$

where ρ_r is the rock density, kg/m^3; ρ_{gstd} is the gas viscosity at standard conditions, kg/m^3; and V_L and P_L are the Langmuir volume, m^3/kg, and Langmuir pressure, Pa, respectively. V_L is equal to the shale matrix's maximum adsorption capacity, and P_L corresponds to half of the shale matrix's maximum adsorption capacity.

The following constraints are imposed to ensure that the governing equations are closed:

$$S_g + S_w = 1, \qquad (60)$$

$$P_w = P_g - P_{cap}, \qquad (61)$$

where P_{cap} is the gas–water capillary pressure, Pa.

3.2. Coupling Method of Matrix–Microfracture–Hydraulic Fracture. An SRV occurs around hydraulic fractures during hydraulic fracturing. Hence, two regions exist in the shale gas reservoir, namely, the SRV and SRV outer regions. Matrix, microfractures, and hydraulic fractures coexist in the SRV region, whereas the SRV outer region only includes the shale matrix, where a single porosity model is applied.

TABLE 2: Parameters used for model verification.

Simulation parameter	Value
Gas reservoir size (/m)	$10^5 \times 10^5 \times 5$
Grid size (/m)	$5 \times 5 \times 5$
Initial pore pressure (/MPa)	40
Gas reservoir temperature (/K)	400
Initial water saturation	0.25
Porosity of matrix	0.1
Porosity of hydraulic fracture	1
Permeability of matrix (/μm^2)	10^{-6}
Permeability of hydraulic fracture (/μm^2)	10
Hydraulic fracture aperture (/m)	10^{-3}

To describe fluid transport in multiple media in the SRV region accurately, MINC were employed to depict the matrix and microfractures, and the hydraulic fractures were addressed based on an embedded discretized fracture using the EDFM.

As illustrated in Figure 2, the main grids inside the SRV region were partitioned into nested grids, in which the outermost grid was used to describe the microfracture. Moreover, the MINC ensured unsteady transport inside the shale matrix. Hydraulic fractures were embedded into the main grids directly via the EDFM, and the hydraulic fracture grids were generated by the segmentation of the main grid boundaries. The grid connection of the matrix–microfracture–hydraulic fracture coupling system is key for calculating the conductivity between adjacent grids and for implementing the fluid transport simulation. In this study, the grid connection relationship was extracted, as shown in Figure 2.

Based on the grid structure, one can classify conductivity into the conductivity between the main grids, the conductivity between the MINC nested grids, and the conductivity associated with hydraulic fractures. Various types of conductivity calculations have been reported in the literature [22].

3.3. Discretization of Governing Equation. The finite volume method was selected to discretize the governing equations owing to its distinct physical meaning and high mesh adaptability. For any grid n (as shown in Figure 2), the mass conservation equations (Eqs. (55) and (56)) are integrated by the volume on grid V_n. Subsequently, the volume integral of the divergence term is converted into the area integral of the boundary flow using the divergence theorem, and the following equations are obtained:

$$\int_{V_n} \frac{\partial \left(\phi \rho_g S_g + \delta_m q_{ads} \right)}{\partial t} dV = \int_{\Gamma_n} - \left(\rho_g \mathbf{v}_g \right) \cdot \mathbf{n} d\Gamma + \int_{V_n} q_g dV, \tag{62}$$

$$\int_{V_n} \frac{\partial (\phi \rho_w S_w)}{\partial t} dV = \int_{\Gamma_n} - (\rho_w \mathbf{v}_w) \cdot \mathbf{n} d\Gamma + \int_{V_n} q_w dV, \tag{63}$$

TABLE 3: Numerical simulation parameters for shale gas reservoir with multistage fractured horizontal well.

Parameter	Value
Gas reservoir size (/m)	$860 \times 350 \times 20$
SRV size (/m)	$720 \times 170 \times 20$
Initial pore pressure (/MPa)	40
Gas reservoir temperature (/K)	400
Initial water saturation	0.22
Gas composition	Methane
Matrix density (ρ_r/(kg·m^{-3}))	2850
TOC content in volume	0.086
Porosity of matrix (ϕ_m)	0.07
Porosity of microfracture (ϕ_{mf})	1
Compression coefficient of microfracture (c_{mf}/MPa^{-1})	0.2
Initial water saturation in microfracture	1
Initial permeability of microfracture (k_{mf0}/μm^2)	4.5×10^{-6}
Stress sensitivity coefficient of microfracture ($a_{s,mf}$/MPa^{-1})	0.1
Microfracture spacing (l_{mf}/m)	5
Porosity of hydraulic fracture (ϕ_{hf})	0.6
Compression coefficient of hydraulic fracture (c_{hf}/MPa^{-1})	0.1
Initial water saturation in hydraulic fracture	1
Stress sensitivity coefficient of hydraulic fracture ($a_{s,hf}$/MPa^{-1})	0.15
Number of hydraulic fracturing stages	8
Spacing of hydraulic fracture stages (/m)	50
Cluster number per stage	3
Cluster spacing (/m)	20
Hydraulic fracture length (/m)	160
Well radius (/m)	0.1
Bottomhole pressure (/MPa)	8
Langmuir volume (V_L/(m^3·kg^{-1}))	0.00258
Langmuir pressure (P_L/MPa)	13.789514

where Γ_n is the boundary of grid n, and $\mathbf{n}$ is the unit normal vector out of the boundary Γ.

The equations above were numerically discretized, and a discretization scheme was obtained as follows:

$$\frac{\left\{ V \left[\phi \rho_g S_g + \delta_m (1 - \phi) q_{ads} \right] \right\}_n^{t+1} - \left\{ V \left[\phi \rho_g S_g + (1 - \phi) q_{ads} \right] \right\}_n^t}{\Delta t}$$
$$= \sum_{m \in \eta_n} \left[\left(\rho_g \lambda_g \right)_{nm+(1/2)}^{t+1} T_{nm}^{t+1} \left(\psi_{gm}^{t+1} - \psi_{gn}^{t+1} \right) \right] + \left(V q_g \right)_n^{t+1}, \tag{64}$$

$$\frac{\left(V \phi \rho_w S_w \right)_n^{t+1} - \left(V \phi \rho_w S_w \right)_n^t}{\Delta t}$$
$$= \sum_{m \in \eta_n} \left[\left(\rho_w \lambda_w \right)_{nm+(1/2)}^{t+1} T_{nm}^{t+1} \left(\psi_{wm}^{t+1} - \psi_{wn}^{t+1} \right) \right] + \left(V q_w \right)_n^{t+1}, \tag{65}$$

(a) Schematic diagram of shale gas reservoir

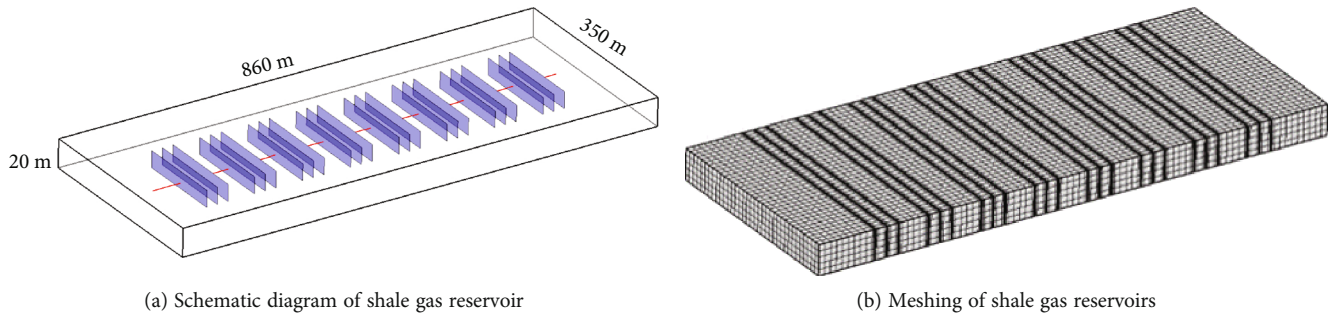(b) Meshing of shale gas reservoirs

FIGURE 16: Schematic diagram of shale gas reservoir with multistage fractured horizontal well.

where η_n represents all grids connected to grid n and subscript $nm + 1/2$ denotes a certain average of meshes n and m at their interface. In general, the harmonic average is used for permeability or conductivity, and the upstream windward-weighted format is used for mobility. The superscripts t and $t + 1$ denote the previous and current time steps, respectively; Δt is the time step, s; λ is the fluid phase mobility, expressed as $\lambda_\beta = k_{r\beta}/\mu_\beta$, $Pa^{-1} \cdot s^{-1}$; and T is the conductivity between different units, m^3. The Newton-Raphson iteration method was applied to solve the highly nonlinear discrete equations (Eqs. (64) and (65)).

4. Results

In this section, the proposed method for investigating gas–water two-phase transport in shale gas reservoirs, which incorporates nanomicroscale effects and rigorous pore-to-core upscaling, is described based on experimental data. The steps are based on the workflow shown in Figure 3.

Step 1. Figures 4 and 5 present the images for IOM and OM obtained from the Sichuan Basin, China, based on SEM and FIB-SEM, respectively. The three-dimensional (3D) IOM digital core and OM digital core measured 11 and $1.6 \,\mu m^3$, and the voxels measured $400 \times 400 \times 400$ for both. The porosities of the IOM and OM were 0.0725 and 0.105, respectively. The gas–water two-phase transport behaviors are obtained by integrating nanomicroscale effects in the IOM pore network, and the associated parameters are summarized in Table 1. The single-phase gas and water permeabilities of the IOM were 2.5×10^{-7} and $2.23 \times 10^{-7} \,\mu m^2$, respectively, whereas those of the OM were 3.36×10^{-8} and $3.02 \times 10^{-8} \,\mu m^2$, respectively. To consider the matrix stress sensitivity in the macroscale simulation, the average pore size changes in the IOM and OM were implemented at the pore scale, as shown in Figure 6. Figure 7 shows the single-phase gas and water permeability with varying pore pressures in the IOM and OM, and the associated parameters are listed in Table 1. The gas–water relative permeability and capillary pressure in the IOM are shown in Figure 8.

Step 2. The IOM/OM pore-scale simulation results above were applied to achieve shale matrix core-scale gas–water two-phase transport. First, a core-scale model measuring $420 \,\mu m \times 420 \,\mu m$ at a TOC of 8.6% was constructed, as shown in Figure 9. Combining the porosity of IOM and OM, as well as the TOC content of the core-scale model,

the porosity of the core-scale shale matrix model of 0.0753 can be determined by the weighted average method. The variations in the core-scale averaged pore radius and single-phase gas and water permeabilities with pore pressure can be derived by combining the pore-scale data, as depicted in Figure 10. Based on the gas–water two-phase transport behavior obtained from the IOM and OM pore network models, the core-scale capillary pressure and gas–water relative permeability were determined, as shown in Figure 11. The core-scale capillary pressure and relative permeability curves shifted to the left, resulting from only single-phase gas flows in the OM patches in the core-scale model. Moreover, the variation of the capillary pressure curve with the pore pressure can be derived using Eq. (53). Figure 12 shows the relative permeability variation at different pore pressures. The effect of stress sensitivity on the shale matrix relative permeability is negligible because the occurrence state of gas–water in the pores remained unchanged, even when the pore size changed with the pore pressure. However, the gas/water effective permeability decreased at different water saturation levels owing to the reduction in the single-phase gas/water permeability during the production process. As for microfracture, a real microfracture from the Sichuan Basin, China, was selected for gas–water two-phase transport simulation. Figure 13 shows the aperture distribution of this real microfracture, and the specific calculation process can be referred to in our previous work [35]. The average aperture of the studied microfracture is $2.08 \,\mu m$. Gas–water two-phase relative permeability and its change with pore pressure are shown in Figure 14. In addition, the capillary pressure of microfracture is much smaller than that of the matrix; hence, the capillary pressure of microfracture is ignored in the macroscale simulation.

Step 3. To date, core-scale gas–water two-phase transport behavior in the shale matrix and microfracture integrating nanomicroscale effects were obtained. To verify the macroscale gas–water two-phase transport model and the solution process, the proposed model was compared with the simulation results using eclipse. Figure 15(a) illustrates the adopted shale gas reservoir conceptual model, which includes one hydraulic fracture at the center. Grid encryption was applied in eclipse to describe the hydraulic fracture, which was described using the EDFM in our model. Table 2 lists the related parameters. Excellent agreement was indicated between Figures 15(b) and 15(c), which justifies the accuracy of the proposed model and solution. Subsequently,
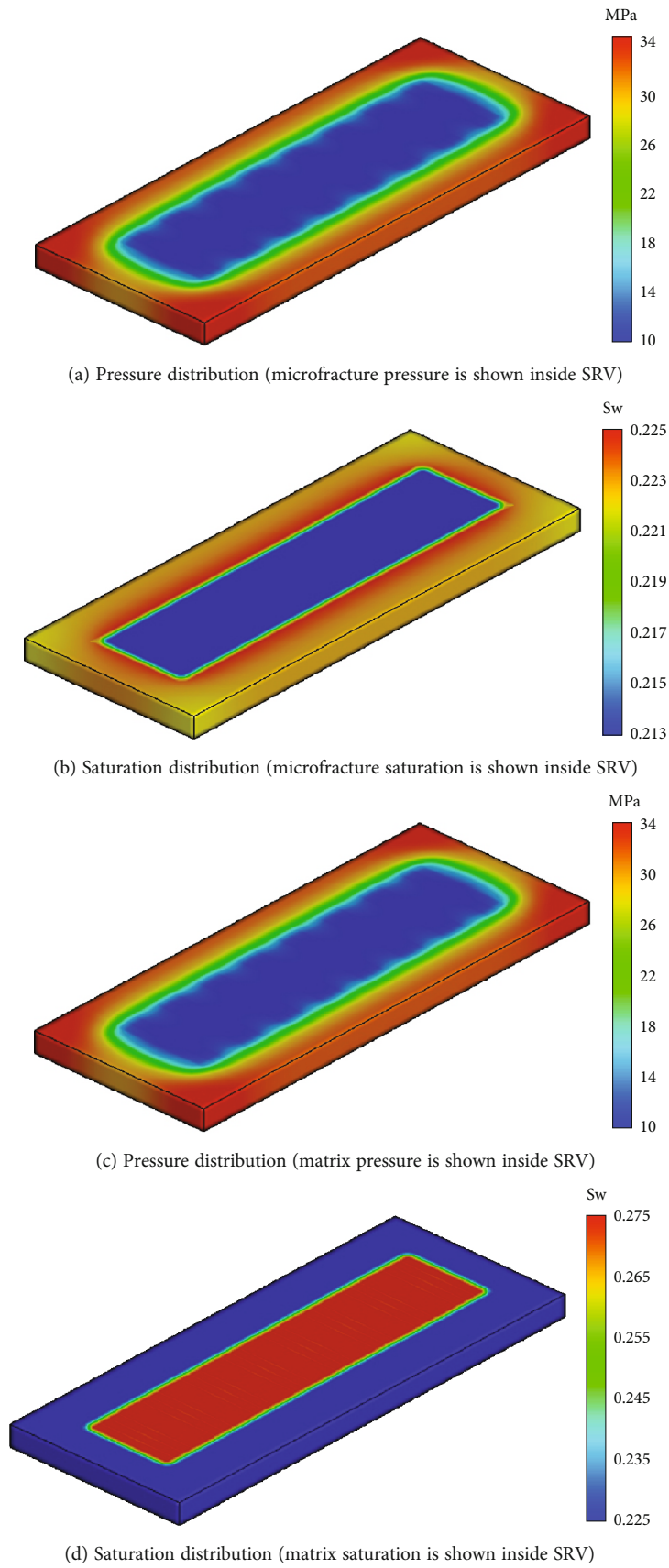
(a) Pressure distribution (microfracture pressure is shown inside SRV)

(b) Saturation distribution (microfracture saturation is shown inside SRV)

(c) Pressure distribution (matrix pressure is shown inside SRV)

(d) Saturation distribution (matrix saturation is shown inside SRV)

FIGURE 17: Pressure and water saturation distribution in shale gas reservoir after 30 years of production.

(a) Gas production rate

(b) Water production rate

(c) Cumulative gas production
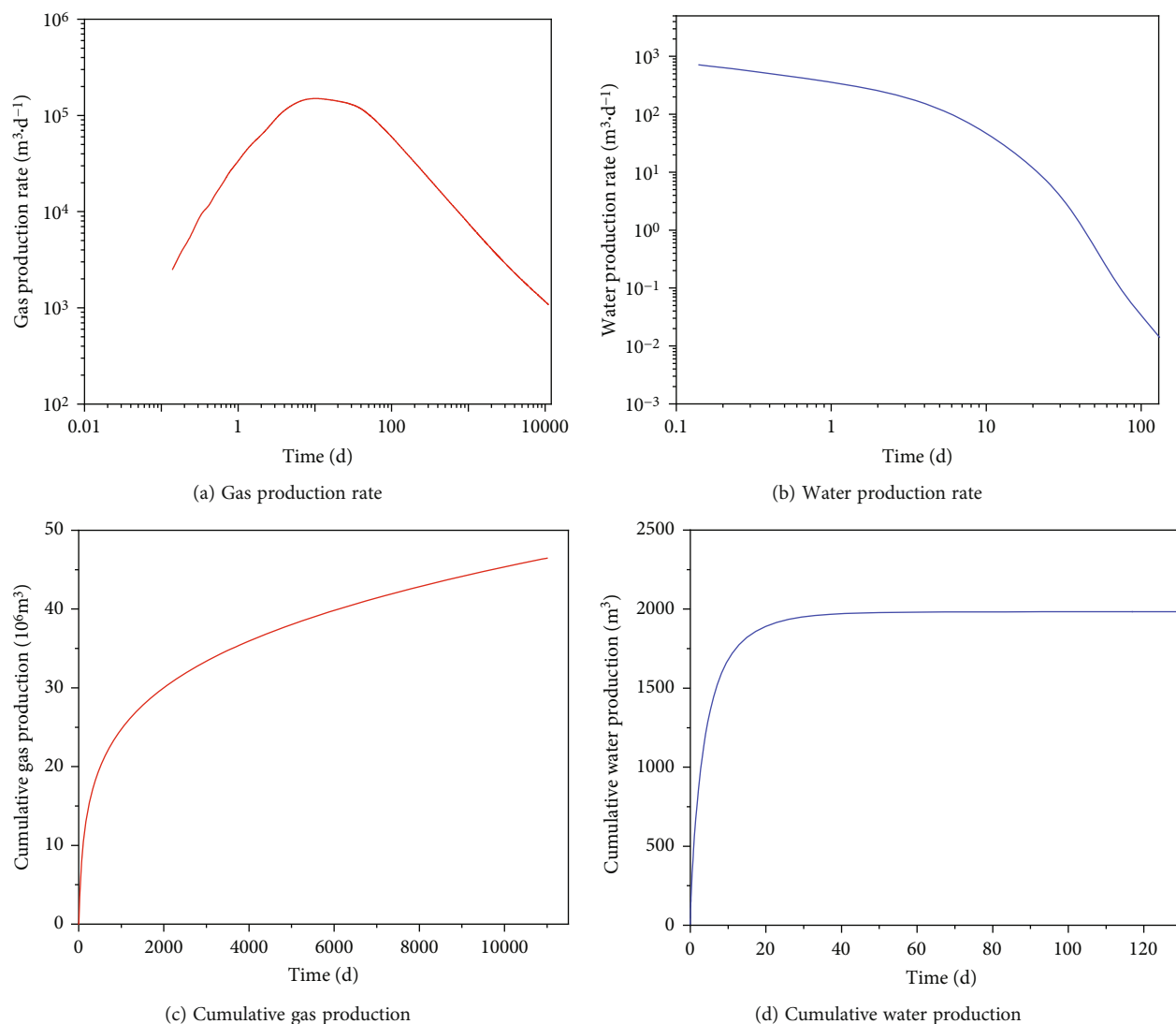
(d) Cumulative water production

Figure 18: Production rate and cumulative production curves of shale gas reservoir.

a gas–water two-phase transport simulation was conducted for a multistage fractured horizontal well in a shale gas reservoir. A summary of the reservoir properties is presented in Table 3. A schematic illustration of a shale gas reservoir with a multistage fractured horizontal well is shown in Figure 16. The SRV zone was established around the hydraulic fractures. MINC were applied to depict the matrix and microfractures inside the SRV, whereas the single porous medium model was used to describe the SRV external area. Structured grids were used for grid division in our model. To depict the fluid flow and distribution around the hydraulic fractures accurately, local grids were encrypted near the embedded discrete fractures, as shown in Figure 16(b). A significant amount of fracturing fluid was injected into the formation during the hydraulic fracturing process. Based on the field data, 10^4 m^3 of fracturing fluid was injected into the gas reservoir in this model, 30% of which existed in the matrix of the SRV inner region and 70% in the hydraulic fracture and microfracture system. Regarding the effect of stress sensitivity, the change in the

pore radius and single-phase gas/water permeability in the shale matrix with pore pressure can be calculated via data interpolation, as shown in Figure 10. The relative permeability in the matrix can be described, as shown in Figure 12, and the capillary pressure can be updated using Eq. (53). The relative permeability of microfracture can be obtained from Figure 14, and the permeabilities of the microfracture and hydraulic fracture were modified using Eq. (54).

Based on Figure 17, the low-pressure area occurred primarily inside the SRV region, and the pressures of the microfracture and matrix in the SRV were similar, thus indicating that the large contact area between the microfractures and matrix resulted in a significant cross-flow. Moreover, the matrix saturation inside the SRV increased to a certain extent. Because the gas pressure between the microfracture and matrix did not differ significantly after short-term production and owing to the action of the matrix capillary pressure, the water pressure in the matrix was lower than that in the microfractures. Consequently, water entered the matrix from microfractures. Figure 18 shows the gas/water
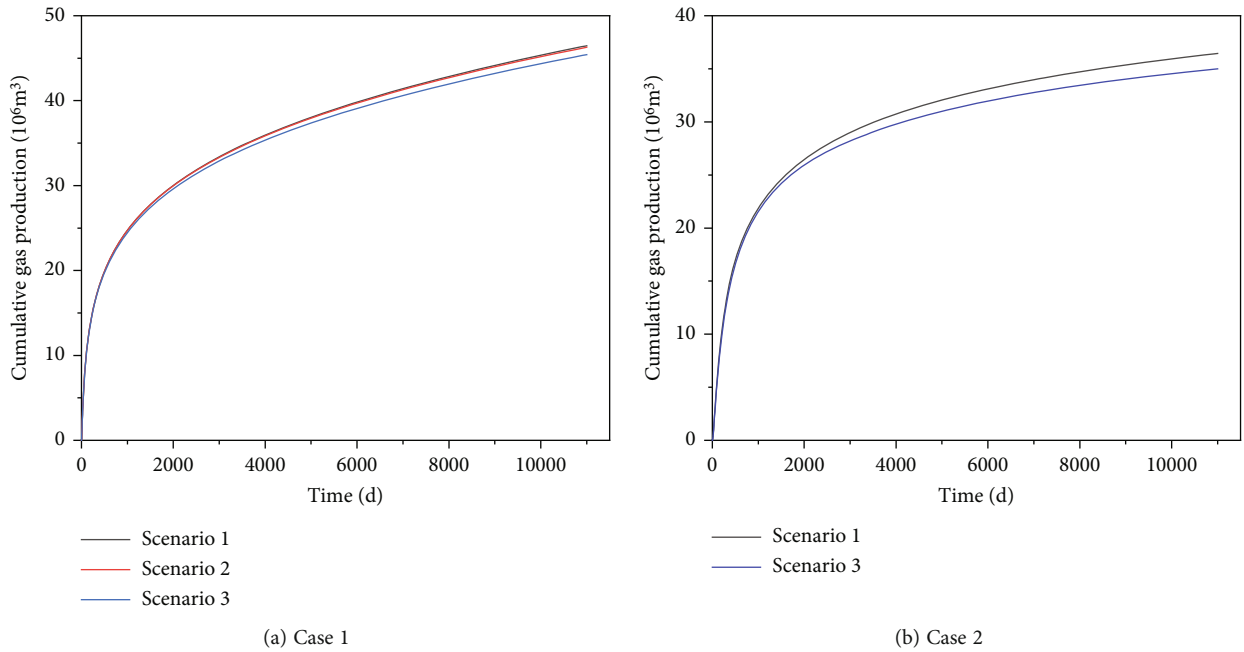
(a) Case 1

(b) Case 2

FIGURE 19: Impact of nanomicroscale effect on shale gas reservoir production.

(a) Gas production rate
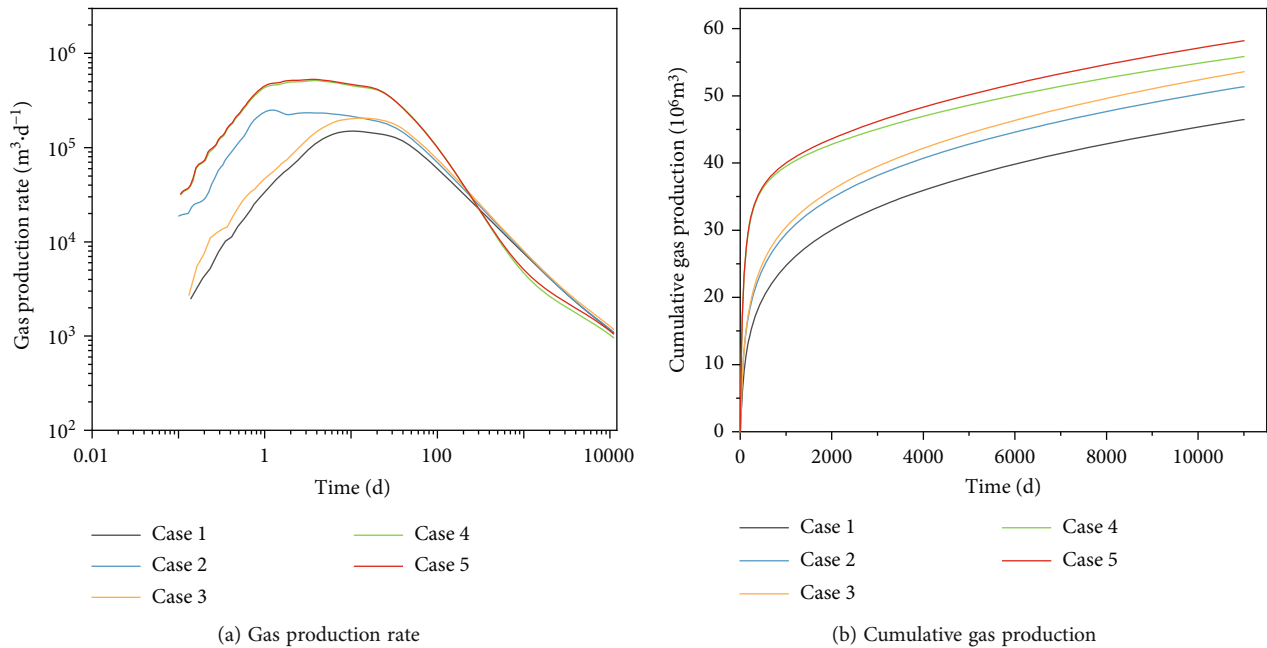
(b) Cumulative gas production

FIGURE 20: Effect of stress sensitivity on gas production rate and cumulative production of shale gas reservoir.

production rate and cumulative production. The flowback stage lasted approximately 40 d, and the flowback rate was 19.8%. At this stage, the gas production increased as water was expelled and then decreased as the pressure decreased in the shale gas reservoir.

4.1. Impact of Nanomicroscale Effect on Production. First, cumulative gas productions were compared under different scenarios: (1) considering full nanomicroscale effects, (2)

only gas phase slip in IOM and Darcy flow in OM, and (3) Darcy flow in both IOM and OM. From Figure 19(a), the production was basically the same under scenarios (1) and situation (2), whereas a certain difference was indicated between scenarios (1) and (3). This indicates that the effect of gas slip was dominant in the IOM. To further analyze the impact of the nanomicroscale effect, the pore size in the pore network model was reduced by half (case 2), and the corresponding mean pore radius was 17.67 nm.
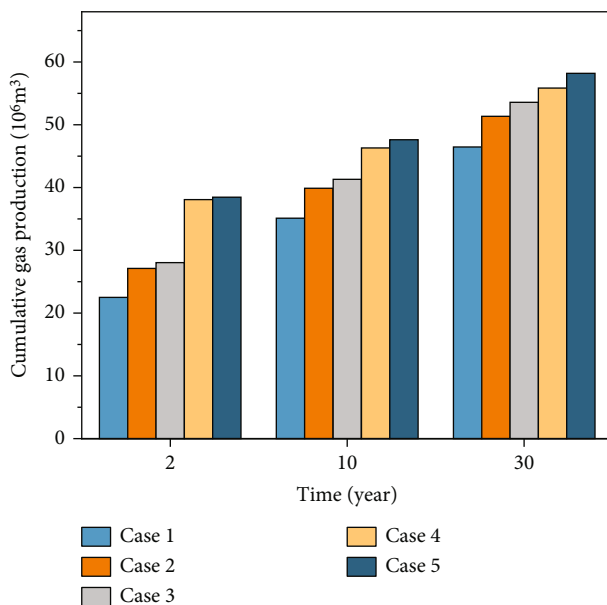
FIGURE 21: Effect of stress sensitivity on gas cumulative production of shale gas reservoir at different stages.

TABLE 4: Relative reduction when considering stress sensitivity of different media compared with the case without considering stress sensitivity at different stages.

Time/year	Relative reduction when considering stress sensitivity of different media compared with the case without considering stress sensitivity		
	Only microfracture stress sensitivity	Only hydraulic fracture stress sensitivity	Only matrix stress sensitivity
2	29.6	27.1	1.0
10	16.2	13.2	2.7
30	11.7	7.9	4.1

(a) Case 1

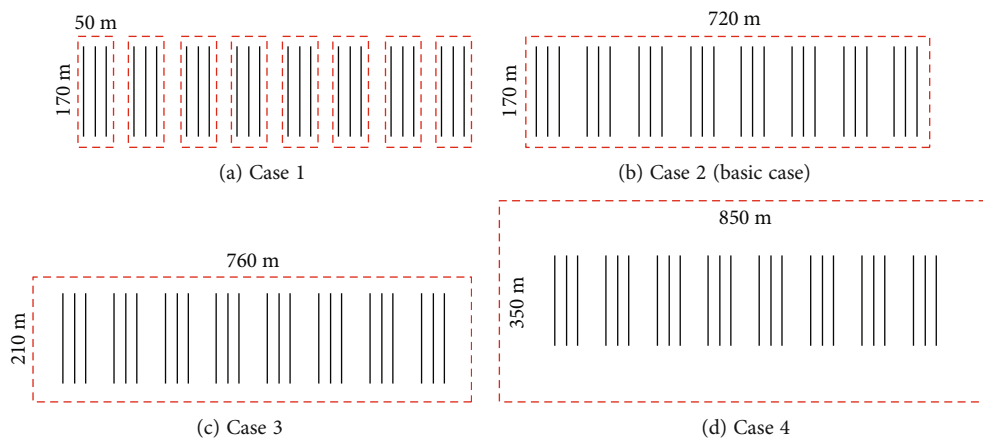(b) Case 2 (basic case)

(c) Case 3

(d) Case 4

FIGURE 22: Schematic diagrams of different SRV areas in shale gas reservoir.

Cumulative gas productions were calculated under scenarios (1) and (3) (Figure 19(b)). Comparing case 1 (mean pore radius of 35.34 nm) with case 2 (mean pore radius of 17.67 nm), the gas production was underestimated by 2.27% and 4.01%, respectively, when the nanomicroscale effect was disregarded. Hence, the smaller the pore size, the more prominent the nanomicroscale effect.

4.2. Effect of Stress Sensitivity on Production. Five cases were implemented to analyze the effect of stress sensitivity on production: (1) considering the stress sensitivity of different media, (2) only considering the microfracture stress sensitivity, (3) only considering hydraulic fracture stress sensitivity, (4) only considering the matrix stress sensitivity, and (5) no stress sensitivity. As shown in Figure 20, disregarding the
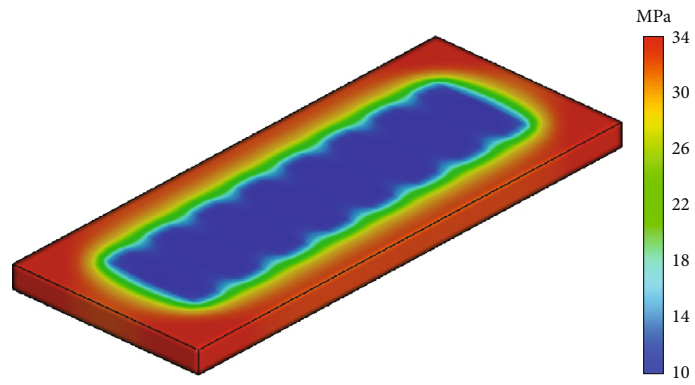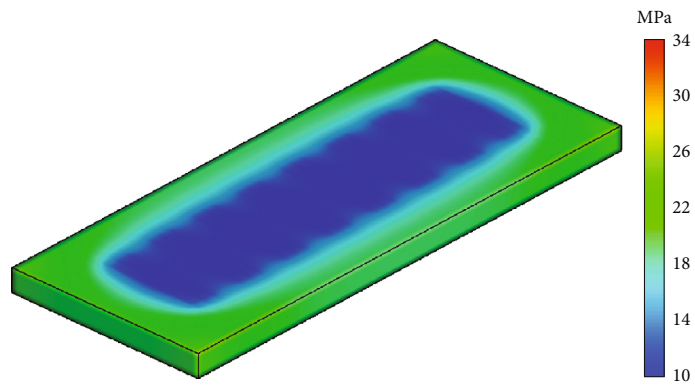
(a) Case 1
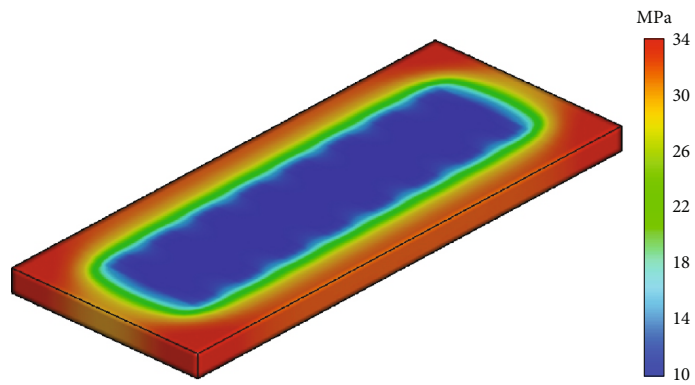
(b) Case 2
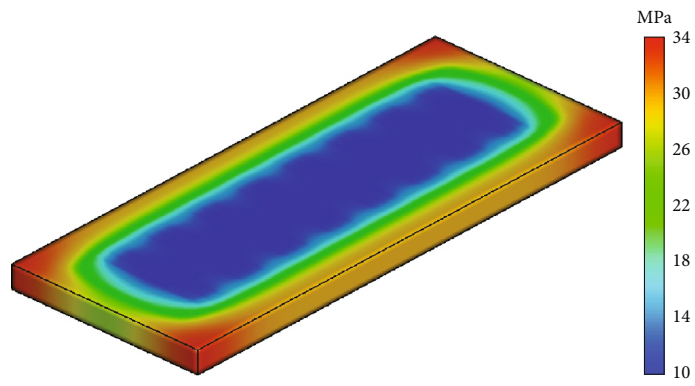
(c) Case 3

(d) Case 4

FIGURE 23: Shale gas reservoir pressure distribution at different SRV areas after 30 years of production.

(a) Gas production rate
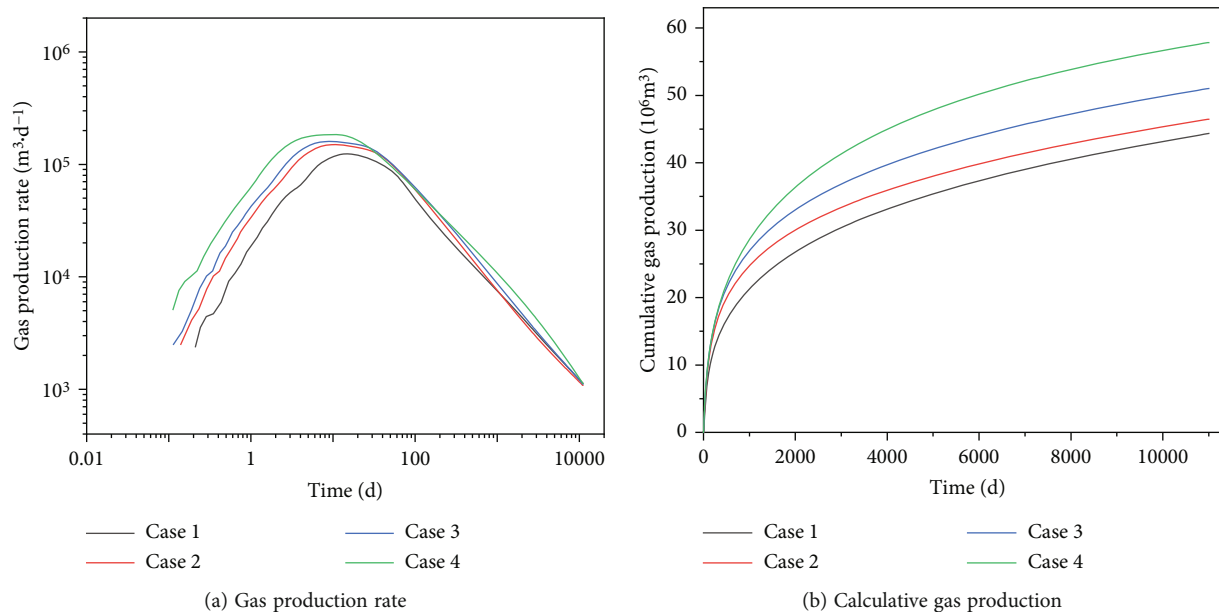
(b) Calculative gas production

FIGURE 24: Effects of different SRV areas on gas production rate and cumulative production of shale gas reservoir.

stress sensitivity of the shale gas reservoir resulted in a significant overestimation of the gas production. Additionally, the stress sensitivity of the microfracture system exerted the greatest effect, whereas the matrix stress sensitivity imposed the least effect.

Figure 21 and Table 4 are constructed to comprehensively examine the effect of stress sensitivity. Figure 21 shows the cumulative gas production at different stages with consideration of the stress sensitivity of different media. Table 4 illustrates the relative reduction when the stress sensitivity of different media was and was not considered. Combining the results of Figures 20(a) and 21 and Table 4, the stress sensitivity of the microfracture and hydraulic fracture system was significant and was primarily reflected at the production initial stage. The gas production rate considering only the matrix stress sensitivity overlapped with that without considering stress sensitivity at the early stage, whereas the effect occurred at the later stage of production. This is because the stress sensitivity of the microfracture and hydraulic fracture was relatively high at the early stage, whereas the pressure drop distributed gradually to the matrix system as production proceeded, thus resulting in a stress-sensitive matrix. In addition, the production rate was higher at the early stage in cases 4 and 5, and energy depletion was evident in the shale gas reservoir, thus resulting in a lower production compared with other cases at later stages (Figure 20(a)).

4.3. Effect of SRV Area Size on Production. Figure 22 shows schematic diagrams of shale gas reservoirs with different SRV sizes (the SRV area is inside the dotted red line). To ensure the same reservoir reserves, the initial water saturation of the matrix inside the SRV was calculated for the four cases under a total fracturing fluid of 10^4 m^3. Figures 23 and 24 show the pressure distribution and gas production after 30 years of production, respectively. The emergence of

microfractures increased the contact area between the fracture and matrix system and increased the gas production rate in the shale matrix, thus resulting in higher gas production rates and cumulative gas production.

5. Conclusions

In this study, a numerical simulation for gas–water two-phase cross-scale transport at the pore, core, and field scales was performed by incorporating multiscale storage spaces and complex fluid transport mechanisms in shale gas reservoirs. The variation in shale gas production was revealed by considering gas–water two-phase nanomicroscale effects. The following conclusions were inferred from this study:

(1) During the production process, pressure drop occurred primarily inside the SRV region, and the pressure of the microfractures in the SRV was similar to that of the matrix. As water was discharged, gas production continued to increase and then gradually decreased as pressure depleted

(2) To some extent, shale gas production was underestimated when nanomicroscale effects were disregarded. The smaller the pore size of the matrix, the greater the error caused by disregarding nanomicroscale effects

(3) A significant error in gas production resulted when the stress sensitivity was disregarded. The stress sensitivities of different media to production can be ranked in descending order as follows: microfractures, hydraulic fractures, and matrices. In addition, the stress sensitivity of microfractures and hydraulic fractures was reflected primarily in the early stages of production, whereas the effect of matrix stress

sensitivity was reflected primarily in the later stages of production

(4) The larger the SRV region of the shale gas reservoir, the larger the contact area between the fracture and matrix system, the higher the gas production from the matrix

The gas–water two-phase cross-scale transport simulation method of shale gas reservoir is proposed in this paper. It is necessary to expand the existing model to the oil–gas–water three-phase multicomponent cross-scale transport model and study the oil–gas–water three-phase transport mechanism under the condition of phase change in shale gas reservoir.

Data Availability

The data underlying this article will be shared on reasonable request to the corresponding author.

Conflicts of Interest

The authors declare that they have no conflicts of interest.

Acknowledgments

References

[1] S. Akilu, E. Padmanabhan, and Z. Sun, "A review of transport mechanisms and models for unconventional tight shale gas reservoir systems," *International Journal of Heat and Mass Transfer*, vol. 175, article 121125, 2021.

[2] J. Huang, T. Jin, M. Barrufet, and J. Killough, "Evaluation of CO_2 injection into shale gas reservoirs considering dispersed distribution of kerogen," *Applied Energy*, vol. 260, article 114285, 2020.

[3] C. Afagwu, M. A. Mahmoud, S. Alafnan, and S. Patil, "Multiscale storage and transport modeling in unconventional shale gas: a review," *Journal of Petroleum Science and Engineering*, vol. 208, article 109518, 2022.

[4] Y. Wang, Z. Dai, L. Chen, X. Shen, F. Chen, and M. R. Soltanian, "An integrated multi-scale model for CO_2 transport and storage in shale reservoirs," *Applied Energy*, vol. 331, p. 120444, 2023.

[5] M. Micheal, W. Xu, J. Jin et al., "A multi-scale quadruple-continuum model for production evaluation of shale gas reservoirs considering complex gas transfer mechanisms and geomechanics," *Journal of Petroleum Science and Engineering*, vol. 213, article 110419, 2022.

[6] A. Li, W. Ding, R. Wang et al., "Petrophysical characterization of shale reservoir based on nuclear magnetic resonance (NMR) experiment: a case study of lower Cambrian Qiongzhusi formation in eastern Yunnan Province, South China," *Journal of Natural Gas Science and Engineering*, vol. 37, pp. 29–38, 2017.

[7] P. Ø. Andersen, "A semi-analytical solution for shale gas production from compressible matrix including scaling of gas recovery," *Journal of Natural Gas Science and Engineering*, vol. 95, p. 104227, 2021.

[8] R. G. Loucks, R. M. Reed, S. C. Ruppel, and U. Hammes, "Spectrum of pore types and networks in mudrocks and a descriptive classification for matrix-related mudrock pores," *AAPG Bulletin*, vol. 96, no. 6, pp. 1071–1098, 2012.

[9] M. E. Naraghi, F. Javadpour, and L. T. Ko, "An object-based shale permeability model: non-Darcy gas flow, sorption, and surface diffusion effects," *Transport in Porous Media*, vol. 125, no. 1, pp. 23–39, 2018.

[10] J. K. Holt, H. G. Park, Y. Wang et al., "Fast mass transport through sub-2-nanometer carbon nanotubes," *Science*, vol. 312, no. 5776, pp. 1034–1037, 2006.

[11] M. Majumder, N. Chopra, R. Andrews, and B. Hinds, "Erratum: nanoscale hydrodynamics: enhanced flow in carbon nanotubes," *Nature*, vol. 438, no. 7070, pp. 930–930, 2005.

[12] B. Bennett, A. Lager, D. K. Potter, J. O. Buckman, and S. R. Larter, "Petroleum geochemical proxies for reservoir engineering parameters," *Journal of Petroleum Science and Engineering*, vol. 58, no. 3-4, pp. 355–366, 2007.

[13] J. Bai, Y. Kang, M. Chen et al., "Impact of water film on methane surface diffusion in gas shale organic nanopores," *Journal of Petroleum Science and Engineering*, vol. 196, p. 108045, 2021.

[14] K. Pruess and T. N. Narasimhan, "A practical method for modeling fluid and heat flow in fractured porous media," *Society of Petroleum Engineers Journal*, vol. 25, no. 1, pp. 14–26, 1985.

[15] D. Y. Ding, N. Farah, B. Bourbiaux, Y.-S. Wu, and C. Wang, "Numerical simulation of low permeability unconventional gas reservoirs," in *Paper presented at the SPE/EAGE European Unconventional Resources Conference and Exhibition*, Vienna, Austria, February 2014.

[16] K. Wang, H. Liu, J. Luo, K. Wu, and Z. Chen, "A comprehensive model coupling embedded discrete fractures, multiple interacting continua, and geomechanics in shale gas reservoirs with multiscale fractures," *Energy & Fuels*, vol. 31, no. 8, pp. 7758–7776, 2017.

[17] C. R. Wilson and P. A. Witherspoon, "Steady state flow in rigid networks of fractures," *Water Resources Research*, vol. 10, no. 2, pp. 328–335, 1974.

[18] C. Louis and W. Wittke, "Etude Experimentale des Ecoulements D'eau Dans Un Massif Rocheux Fissure, Tachien Project, Formose," *Geotechnique*, vol. 21, no. 1, pp. 29–42, 1971.

[19] J. Noorishad and M. Mehran, "An upstream finite element method for solution of transient transport equation in fractured porous media," *Water Resources Research*, vol. 18, no. 3, pp. 588–596, 1982.

[20] S. H. Lee, M. F. Lough, and C. L. Jensen, "Hierarchical modeling of flow in naturally fractured formations with multiple length scales," *Water Resources Research*, vol. 37, no. 3, pp. 443–455, 2001.

[21] W. Yu, K. Wu, M. Liu, K. Sepehrnoori, and J. Miao, "Production forecasting for shale gas reservoirs with nanopores and complex fracture geometries using an innovative nonintrusive EDFM method," in *Paper presented at the SPE Annual Technical Conference and Exhibition*, Dallas, Texas, USA, September 2018.

[22] J. Huang, T. Jin, Z. Chai, M. Barrufet, and J. Killough, "Compositional simulation of fractured shale reservoir with distribution of nanopores using coupled multi-porosity and EDFM method," *Journal of Petroleum Science and Engineering*, vol. 179, pp. 1078–1089, 2019.

[23] R. Zhang, J. Wu, Y. Zhao, X. He, and R. Wang, "Numerical simulation of the feasibility of supercritical CO_2 storage and enhanced shale gas recovery considering complex fracture networks," *Journal of Petroleum Science and Engineering*, vol. 204, article 108671, 2021.

[24] F. Zhang and H. Emami-Meybodi, "A semianalytical method for two-phase flowback rate-transient analysis in shale gas reservoirs," *SPE Journal*, vol. 25, no. 4, pp. 1599–1622, 2020.

[25] P. Cao, J. Liu, and Y.-K. Leong, "A multiscale-multiphase simulation model for the evaluation of shale gas recovery coupled the effect of water flowback," *Fuel*, vol. 199, pp. 191–205, 2017.

[26] N. Farah, M. Delorme, D. Y. Ding, Y. S. Wu, and D. Bossie Codreanu, "Flow modelling of unconventional shale reservoirs using a DFM-MINC proximity function," *Journal of Petroleum Science and Engineering*, vol. 173, pp. 222–236, 2019.

[27] J. M. Rine, E. Smart, W. Dorsey, K. Hooghan, and M. Dixon, "Comparison of porosity distribution within selected North American shale units by SEM examination of argon-ionmilled samples," *Electron Microscopy of Shale Hydrocarbon Reservoirs*, vol. 102, pp. 137–152, 2013.

[28] A. F. Gangi, "Variation of whole and fractured porous rock permeability with confining pressure," *International Journal of Rock Mechanics and Mining Sciences & Geomechanics Abstracts*, vol. 15, no. 5, pp. 249–257, 1978.

[29] I. Shovkun and D. N. Espinoza, "Coupled fluid flowgeomechanics simulation in stress-sensitive coal and shale reservoirs: impact of desorption-induced stresses, shear failure, and fines migration," *Fuel*, vol. 195, pp. 260–272, 2017.

[30] A. Beskok and G. E. Karniadakis, "Report: a model for flows in channels, pipes, and ducts at micro and nano scales," *Microscale Thermophysical Engineering*, vol. 3, no. 1, pp. 43–77, 1999.

[31] T. Patzek and D. B. Silin, "Shape Factor and Hydraulic Conductance in Noncircular Capillaries: I. One- Phase Creeping Flow," *Journal of Colloid and Interface Science*, vol. 236, no. 2, pp. 295–304, 2001.

[32] D. Wang, J. Yao, Z. Chen, W. Song, and H. Sun, "Multiphase flow model from pores to cores in organic-rich shale," *Journal of Petroleum Science and Engineering*, vol. 194, article 107317, 2020.

[33] T. Al-Shemmeri, *Engineering Fluid Mechanics*, Bookboon, 2012.

[34] D. Wang, J. Yao, Z. Chen, W. Song, and H. Sun, "Image-based core-scale real gas apparent permeability from pore-scale experimental data in shale reservoirs," *Fuel*, vol. 254, article 115596, 2019.

[35] D. Y. Wang, J. Yao, Z. X. Chen, H. Sun, and W. Song, "Gaswater two-phase transport properties in shale microfractures," *Chinese Science Bulletin*, vol. 64, pp. 3232–3243, 2019.

[36] Y. Li, Y. Wang, and H. Ma, "Pressure decline analysis on natural closure of cracks after multistage fracturing in shale gas reservoir," *Petroleum Geology and Recovery Efficiency*, vol. 23, no. 2, pp. 98–102, 2016.